University of South-Eastern Norway
Faculty of Technology, Natural Sciences and Maritime Sciences

Doctoral dissertation no. 2
2018

Ying Zhao

Surface plasmonics analysis and photoelectrochemical properties of Au/TiO_2 nanosystems

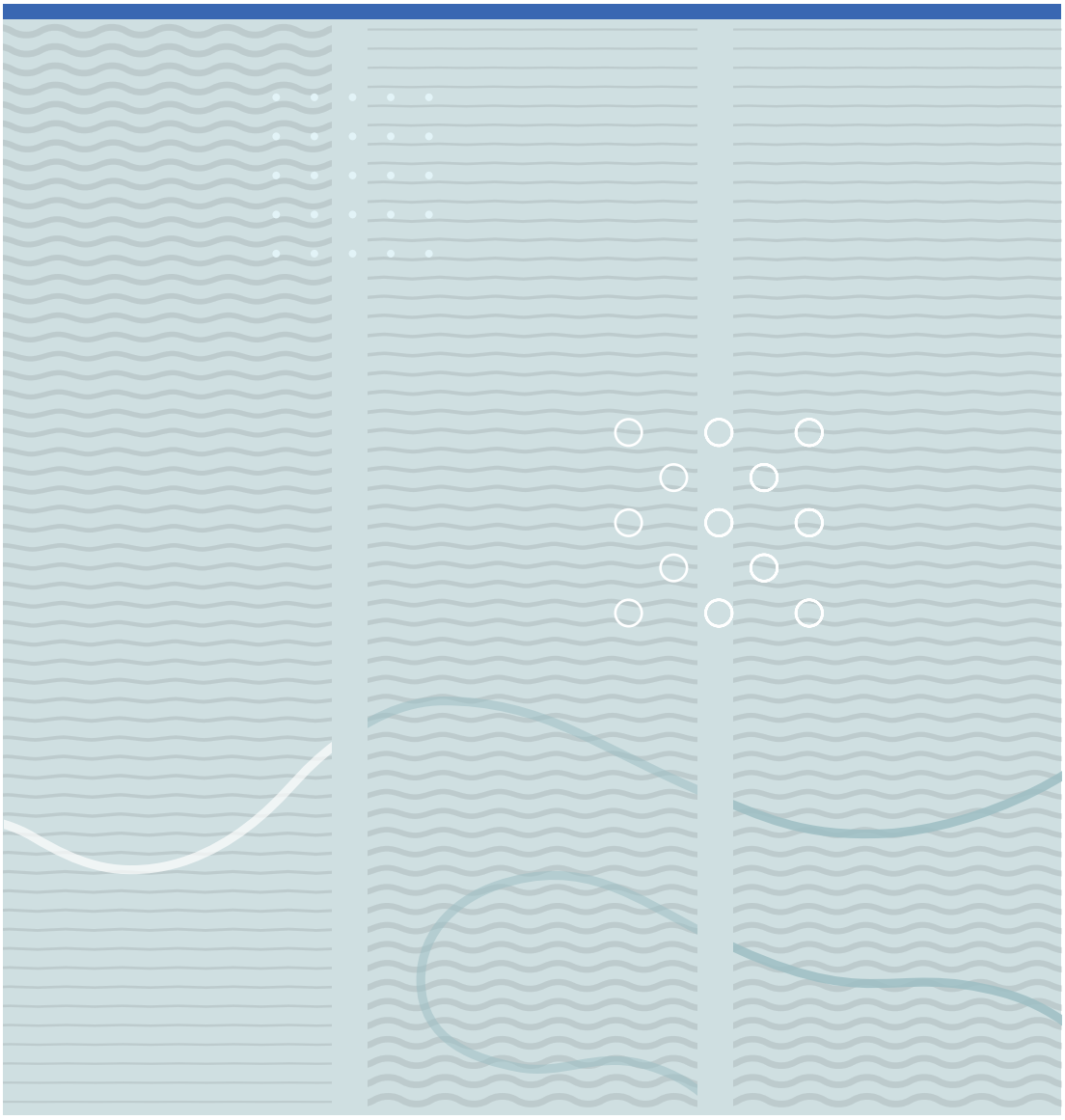

Ying Zhao

Surface plasmonics analysis and photoelectrochemical properties of Au/TiO_2 nanosystems

A PhD dissertation in
Applied Micro- and Nanosystems

Faculty of Technology, Natural Sciences and Maritime Sciences
University of South-Eastern Norway
Borre, 2018

Doctoral dissertations at the University of South-Eastern Norway no. 2

ISSN: 2535-5244(print)
ISSN: 2535-5252 (online)

ISBN: 978-82-7860-325-3 (print)
ISBN: 978-82-7860-327-7 (online)

Print: University of South-Eastern Norway

Preface

This thesis is submitted in partial fulfilment of the requirements for the degree of Philosophiae Doctor (Ph.D.) at the University College of Southeast Norway (USN). The thesis is based on the work carried out at the Department of Microsystems (IMS) from August 2012 to August 2017. This work is financially supported by KD program at University College of Southeast Norway and Norwegian PhD Network on Nanotechnology for Microsystems, which is sponsored by the Research Council of Norway, Division for Science, under contract no. 221860/F40.

My deepest gratitude goes first and foremost to my supervisors, Professor Kaiying Wang and Professor Nils Høivik, for their excellent guidance and constant encouragement during this process. They have walked me through all the stages of the Ph.D. process, and shared my joy for the synthesis, the hope for good results and the sadness and tiredness with each failed attempt. Without their support, I would never come to this final point.

Secondly, I would like to thank Kang Du who has been working on a related project in the same group with me. It was always helpful to talk and share ideas with you. To my other colleagues take charge of the laboratory, Zekija, Thomas, Ragnar and Anh-Tuan, thank you for all the assist you had been offering me during my experiment.

Last but not least, my family deserve a particular note of thanks: my parents, thank you for always being there for me, and I want you to know that I will do the same for you; my husband and my son, thank you for providing me a harbour of love and happiness where I can forget all the struggle and frustration.

Thanks to all the Ph.D. students for your company and I hope you enjoy your reading.

Abstract

This thesis focuses on investigation of photoelectric and photoeletrochemical (PEC) performance of TiO_2 nanotube based photoelectrodes. Surface plasmonic resonance (SPR) have been studied by theoretical analysis, fabrication and optimization of nanocrystallines Au on TiO_2 nanotube arrays for facilitating both photoactivity and carrier transfer.

Numerical analysis of surface plasmonic resonance on different Au/TiO_2 nanostructures is a focal point of the study. Finite element analysis was performed through electromagnetic wave module under frequency domain. Simulation results agree well with experimental results. Meanwhile, it is revealed by simulation that plasmonic Au-nanoring structure can originate deeper and more uniformly distributed near-surface electric field within TiO_2 nanotubes as compared to Au-nanoparticles. Furthermore, a novel optical structure where Au nanodisks are embedded in titanium dioxide nanohole arrays was proposed based on analogous numerical study. Simulation demonstrates five to seven times light absorption enhancement at resonant wavelength of 700 - 800 nm despite of varied reception angles from 0 to 45 degrees. Broad absorption bandwidth is possible by varying the thickness of the embedded Au layer. Such structure will improve the optical absorption performance of TiO_2 nanostructure in the visible light region while maintaining the UV absorption by TiO_2 material. Fabrication process was introduced in theory to realize the nanostructure.

For experimental study, self-ordered TiO_2 nanotubes were synthesized via electrochemical anodization with good control of dimension and phase. Au nanoparticles and nanoring structures were subsequently formed on TiO_2 nanotubes via magnetron sputtering for different time intervals. Au-coated TiO_2 photoanode exhibits extended light absorption spectrum to the visible light region. PEC measurement results indicate nearly three times accelerated charge transfer rate and four times enhanced photocurrent response after proper amount of Au coating. These improved performance of Au/TiO_2 nanostructures are all attributed to surface

plasmonic resonance which is generated at the interface of Au and TiO_2. In addition, transient current response shows different ramp-up behaviour at the onset of illumination. Such distinct performance could be related to how the SPR-induced electric field is distributed in the vicinity of Au/TiO_2 interface and how the charge carriers travel and recombine along the longitudinal dimension of the TiO_2 layer.

Papers omitted from online publication due to publisher's restrictions

List of publications

Journal Papers

Article 1

Zhao, Y., Hoivik, N., & Wang, K. (2016). Recent advance on engineering titanium dioxide nanotubes for photochemical and photoelectrochemical water splitting. *Nano Energy*, 30, 728-744. DOI: 10.1016/j.nanoen.2016.09.027

Article 2

Zhao, Y., Hoivik, N., Akram, M.N., & Wang, K. (2017). Study of plasmonics induced optical absorption enhancement of Au embedded in titanium dioxide nanohole arrays. *Optical Materials Express*, 7(8), 2871-2879. DOI: 10.1364/OME.7.002871

Article 3

Zhao, Y., Hoivik, N., & Wang, K. (2018). Microstructure and photoelectric response of gold nanocrystalline on TiO_2 nanotube arrays. *The Journal of Physical Chemistry C,* 122(14), 7877-7884. DOI: 10.1021/acs.jpcc.7b08608

Conference Papers

Article 1

Zhao, Y., Hoivik, N., & Wang, K. (2014). Study of TiO_2 nanotube formation mechanisms by simulation on electric domain. ECS Transactions, 61(36), 9-13. DOI:10.1149/06136.0009ecst

Article 2

Zhao, Y., Hoivik, N., & Wang, K. (2014). Photoconductivity of Au-coated TiO_2 nanotube arrays. IEEE International Conference on Nanotechnology, Toronto, Canada, August 18-21. DOI: 10.1109/NANO.2014.6967993

Papers not enclosed in the thesis

Article 1

Zhao, Y., Du, K., Liu, G., San, H., Hoivik, N., & Wang, K. (2013). Study of electrical field distribution and growth of gradient-arrayed TiO_2 nanotubes by electrochemical anodization. IEEE International Conference on Nanotechnology, Beijing, China, August 5-8. DOI: 10.1109/NANO.2013.6721043

Article 2

Nazareno, H.C., Zhao, Y., & Wang, K. (2014). Photoelectrochemical properties of nanocomposites MoS_2 -TiO_2 prepared by high energy ball milling. IEEE International Conference on Nanotechnology, Toronto, Canada, August 18-21. DOI:10.1109/NANO.2014.6968022

List of abbreviations

1D	One-dimensional
AEF	Absorption enhancement factor
BG	Band gap
CB	Conduction band
CE	Counter electrode
CPE	Constant phase element
DI	Deionized
DOS	Density of states
e^-	electron/negative charge
ECM	Equivalent circuit model
EDX	Energy dispersive x-ray spectroscopy
EIS	Electrochemical impedance spectroscopy
EM	Electromagnetic
FAD	Field assisted dissolution
FAO	Field assisted oxidation
FEA	Finite element analysis
FE-SEM	Field-emission scanning electron microscopy
FFT	Fast Fourier transform
h^+	hole/positive charge
HER	Hydrogen evolution reaction
I-V	Current-Voltage
OER	Oxygen evolution reaction
PC	Photocatalytic
PEC	Photoelectrochemical
PML	Perfectly matching layers
SHT	Solar-to-hydrogen
SPR	Surface plasmonic resonance
TE	Transverse electric
TM	Transverse magnetic

TNPA	TiO_2 nanopillar array
TNPs	TiO_2 nanoparticles
TNTA	TiO_2 nanotube array
TNTs	TiO_2 nanotubes
UV	Ultraviolet
WE	Working electrode
XRD	X-ray diffraction

Summary of published scientific work

Journal paper 1: This is a review on the recent advances on exploration of TiO_2 nanotubes (TNTs)-based photoelectrodes as well as their applications for water splitting systems. Model and conventional strategies for modification of nanotubes morphology and TiO_2 materials have been summarized in terms of improvement on TNTs-based water splitting systems. This paper aims at providing a broad insight into the TiO_2 nanotubes serving as photoelectrode for various but especially hydrogen evolution application.

Journal paper 2: This study has proposed a novel TiO_2 nanohole arrays structure embedded with Au nanodisks as plasmon generator for the purpose of optical absorption enhancement. Paper has focused on the numerical study of absorption enhancement on the proposed structure and provided a possible approach for fabrication process. Results shown that additional gold fillings inside TiO_2 nanohole arrays can improve absorption at a wide reception angle and promote a strong surface plasmonic effect at plasmonic frequency (λ = 700 - 850 nm for the selected periodicity and material described in this study) while still maintaining the same absorption in the low wavelength range.

Journal paper 3: A facile synthesis of Au nanoring structures have been carried out where size and distribution are accurately controlled and regulated by dimension of the nanotube arrays on large-scale substrates (spanning several square mm). The obtained Au nanoring-TiO_2 systems with controllable thickness provide promising PEC performance. We further conducted a series of numerical studies to research the correlation between the difference in SPR effect induced from Au nanoparticles and nanorings. The good agreement between finite element analysis (FEA) and experimental results (qualitatively) verifies the validity of our numerical study. Therefore, this study provides a new perspective on SPR effect for the enhanced photocurrent response on TiO_2 nanotube arrays.

Conference paper 1: A study on formation mechanisms of TiO_2 nanotube by using COMSOL simulation of electric domain has been reported in this paper. The models are built according to existing field-assisted dissolution (FAD) model of the growth of highly self-organized TiO_2 nanotubes structures. The simulation of morphological evolution over time provides a well forming process for smooth hemispheric bottom at the end of the nanotubes. Current density distribution through both initial nanocracks and as-formed nanopores suggests that the H^+ ions during the FAD process are derived from the field-assisted oxidation process rather than from the electrolyte.

Conference paper 2: In this paper, we report the fabrication and photoconductivity of Au-doped titanium nanotube array (TNTA). Scanning electron microscope with energy dispersive x-ray spectroscopy (SEM-EDX) indicates that diameter of as-prepared TNTs is distributed from 80 to 160 nm. The as-prepared TNTA shows an amorphous structure and completely converted into anatase phase after annealing at 450 ^oC for 3 hours. A sandwich-type (Indium tin oxide glass/ Au-doped TNTA/Ti) device was assembled for photoelectric characterization. Photocurrent of Au-doped TNTA is increased to 28.7 mA at applied voltage of 1 V under ultra-violet radiation as compared with that of pristine TNTA device (0.7 mA). A phenomenal sketch is given to understand enhancement of the photoconductivity.

Table of contents

1 Introduction

The steady increase of energy consumption coupled with environmental pollution has promoted a vast of research in generating renewable energy [1]. Solar photoelectrochemical (PEC) hydrogen production is a promising technologie that could provide a clean and cost-effective energy carrier by taking advantage of the ~ 120,000 terawatts of radiation that continually strikes the surface of the earth [2]. TiO_2 nanotube array (TNTA), as a potential candidate for PEC water splitting application, has drawn great attention due to its outstanding anti-corrosion feature and the fact that TiO_2 is abundant in earth [3]. However, the large band gap (BG) of TiO_2 material requires that it must be modified in order to utilize the large portion of visible light in solar spectrum. To this respect, SPR generated via noble metals is effective and stable when coupled to TiO_2 [4-6].

1.1 PEC water splitting

The pioneering work on PEC water splitting was reported in 1972 by Fujishima and Honda [7]. In 1998, Khaselev and Turner [8] demonstrated a PEC device with solar-to-hydrogen conversion efficiency of 12.4%, which highlights the great potential of PEC water splitting technology for future renewable energy generation.

1.1.1 Working mechanism

A typical PEC water splitting system consists of a photoactive semiconductor material (working electrode - WE), a back contact, electrolyte, a metal counter electrode (CE) and external circuit (metal wires and/or bias source). Optionally, co-catalyst, sacrificial agent and modification materials can be included in the system to achieve better PEC performance. Figure 1 illustrates fundamental processes and energy requirements in a PEC water splitting device [2]. When the semiconductor photoanode is irradiated by photons with energy that is higher than its BG, electron/hole (e^-/h^+) pairs are generated within the semiconductor material. These charge carrier pairs are then separated and driven to opposite directions within the semiconductor. The positive charges (h^+) tend to migrate to the semiconductor/electrolyte interface and drive the

oxygen evolution reaction (OER), while the negative ones (e^-) travel to CE through back contact and external circuit to drive hydrogen evolution reaction (HER).

The notations used in Figure 1 are as follows [2]:

V_{ph} – the actual driving force (photovoltage) for water splitting, which ideally is equal to the BG of the semiconductor photoelectrode, but practically is less due to losses;

ΔE^0 – thermodynamic voltage for water splitting;

$OP_{HER/OER}$ – overpotentials associated with driving the kinetics of HER/OER at the solid-liquid interface.

To initiate the PEC reaction, V_{ph} cannot be less than the sum of OP_{HER}, OP_{OER} and ΔE^0, which means that BG of the semiconductor for photoanode must be sufficiently larger than OP_{HER} + OP_{OER} + ΔE^0. Addition of co-catalyst to WE/CE can help to reduce OP_{OER}/OP_{HER}, allowing for the application of narrow-banded semiconductor to PEC devices.

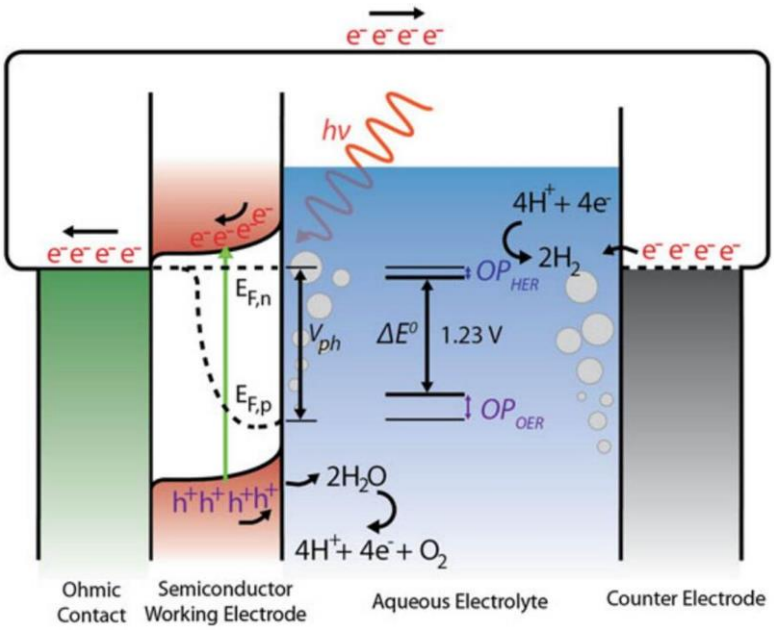

Figure 1 Scheme of typical PEC water splitting process and energy required during the process [2]

1.1.2 PEC *vs.* Photocatalytic (PC) water splitting

The boundary between the definition of PEC and PC in terms of water splitting can be ambiguous in many existing articles [9, 10]. In the literal sense, PEC is more general and includes PC. However, in most studies, a more commonly used definition of these two words is as follows:

PEC system – a fixed-electrode design (as is shown in Figure 1) where the light-absorber materials, resembling that of a solar-cell light absorber, are immersed into an aqueous electrolyte [11].

PC system – a particle-suspension system where the particles are free to move in their mixture with the electrolyte and are not incorporated as part of a membrane to separate sites of anodic and cathodic redox chemistry [11].

Table I Brief comparison between PEC and PC water splitting processes in terms of different aspects.

	PEC water splitting	PC water splitting
Electrical Bias	Optional	Not Applicable
Co-catalyst	Optional	Almost necessary for HER [12, 13]
Gas separation and collection	OER and HER happen on photoanode and photocathode, respectively, easy to be separated and collected	OER and HER separation is possible via application of additional separator and/or redox couple, which is very complex [11]
Sustainability	Waste electrodes can be easily collected and recycled	Difficult to clean and collect all the particle suspensions from the aqueous solution

A brief description and comparison of PEC and PC water splitting systems are listed in Table I. The purpose of the table is to better understand the difference between the working and operation principles of these two systems. According to Turner et al. [14], overall solar-to-hydrogen (STH) efficiency is the single value by which all PEC devices can be reliably ranked against one another. In addition, valid calculation of STH requires no sacrificial reagent and no separated compartment in the device. However, for the sake of investigating the reaction kinetics and discovering the best-performing photoactive materials for hydrogen generation, a significant number of researches did

not report the STH data. To date, efficiencies of 12.4% STH for a Tandem cell [8] and 18.3% STH for a multijunction cell [15] have been achieved.

1.1.3 Overview of semiconductor materials for PEC water splitting

High-efficient hydrogen production by means of PEC water splitting requires that the semiconductor system must : (1) be able to utilize a large portion of solar light, (2) possess band edges that straddle the hydrogen and oxygen redox potentials, (3) sufficiently transfer charge carriers to solution and (4) resist corrosion in aqueous electrolytes and under photo-irradiation [2]. To discover semiconductor systems that meet the aforementioned criteria, intensive investigations within material science and other disciplines have been carried out [4, 8, 9, 16-28].

Commonly used semiconductors and their band edge distribution, as well as the energy levels of frequently involved metal materials with regard to PEC water splitting are listed and shown in Figure 2 [29]. Classic semiconductors, such as CdS, Fe_2O_3 and WO_3 in black and green group in the figure, have narrow BG which is favourable in terms of making the best use of incident photons. However, CdS is found to be unstable owing to the photodissociation that results from self-oxdiation by holes [1]. Fe_2O_3 and WO_3, on the other hand, are incapable of driving the one-step overall water splitting process due to their insufficiently low CB level [1]. On the contrast, large BG (> 3.0 eV) semiconductors with metal cations are developed for water splitting under UV and/or visible light. As early as the year 1985, photoelectrochemical cell using SiC and Pt electrodes with energy conversion efficiency to H_2 of 0.4 % was reported without any external bias [30]. In 2009, Yang *et al.* synthesized nitrogen-doped ZnO nanowire arrays for water splitting and achieved a photo-to hydrogen coversion efficiency of 0.15 % at an applied potential of +0.5 V versus Ag/AgCl [18]. Two year later, Iwashina and Kudo reported the Rh-doped $SrTiO_3$ photocatalyst electrode which showed a photo-to-current efficiency of 0.18% at 420 nm under an applied potential of -0.7 V vs Ag/AgCl [31]. Liu *et al.* developed and demonstrated a ZnO/ZnS/Au composite photoanode in 2015 with STH of 0.21 % in the white and visible light region [32].

Among all the large BG semiconductor materials, TiO_2 is the most intensively studied material [3, 4, 23, 29].

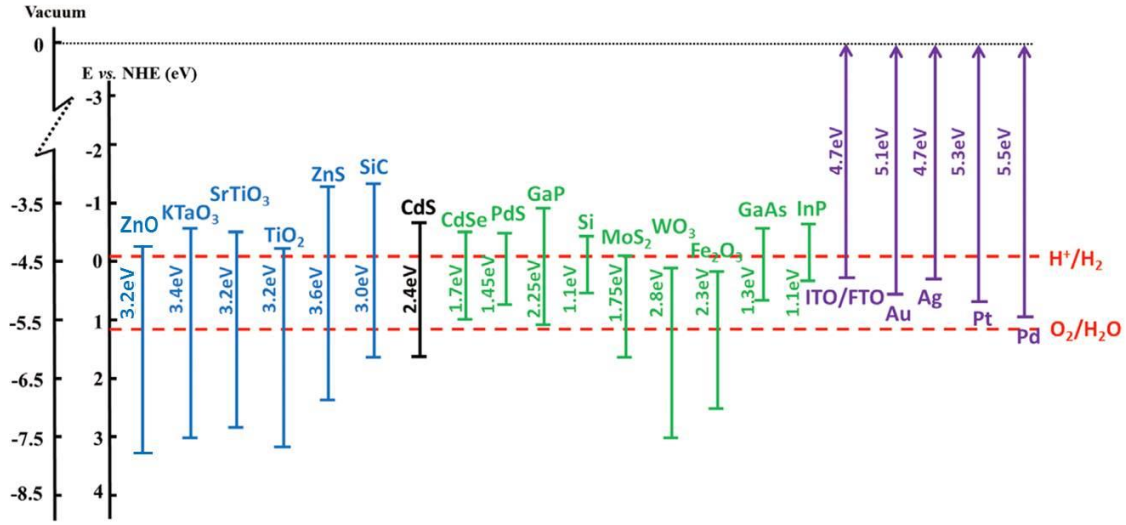

Figure 2 Energy levels of commonly used semiconductors (blue, black and green), noble metals (purple) and redox potential of splitting water into H_2 and O_2 (red) [29].

1.2 TiO_2 nanotubes as photoanode

1.2.1 Why TiO_2 nanotubes

Although efficiencies between 12.4% and 18.3% have been achieved on specific PEC devices, the performance cannot be sustained because the photoelectrode materials are not stable under operating conditions and undergo photocorrosion [9]. Rather than discovering or synthesizing new semiconductor materials, an alternative strategy to overcome the stability issues is to exploit scaling laws and specific effects at the nanoscale to enhance the efficiency of existing semiconductors and metal oxides [9]. The advantages of using nanomaterials for solar energy conversion was first demonstrated on the nanostructured dye-sensitized photoelectrochemical cell by Gratzel *et al*. in 1991 [33]. From then on, nanoscale photoelectrochemistry became a modern research area. Osterloh [9] has pointed out the concomitant pros and cons of nanostructured photoelectrodes and photocatalysts, which include quantum size confinement, short pathway for collection of charge carriers but slow interparticle

transportation, multiple exciton generation but at the same time high chance of recombination, improved light distribution but low absorbed photon flux.

As an abundant mineral in nature, TiO_2 (common forms are rutile, anatase and brookite) attracts lots of attention with regard to PEC water splitting as well as other PEC applications due to its non-toxic and corrosion-resistant features. Although TiO_2 possesses a large BG ~ 3 eV, it has a suitable band-edge position which makes it a proper material for splitting water into hydrogen and oxygen [3, 9, 29]. Conventional TiO_2 nanoparticles (TNPs) suffer from high amount of charge losses due to the electron hopping between particles [3, 34] and therefore are unfavourable for PEC activities where fast charge carrier separation and transfer is required. The utilization of one-dimensional (1D) nanostructures has helped to solve the problem. Among all the 1D nanostructured TiO_2, such as nanorod, nanowire, nanopillar and *etc.*, TNTs provide the maximized specific surface area due to its hollow structure. At the same time, TNTs offers significantly shorter carrier diffusion pathway along the tube wall and allows for a much higher control of chemical and physical behaviour [3].

1.2.2 Synthesis of TiO_2 nanotubes

The first report about synthesis of TiO_2 nanotubes goes back to 1995. Hoyer, who employed porous aluminium oxide as template and electrochemically deposited TiO_2 into the mould, successfully synthesized TNTA by the so-called template-assisted method [35]. The template-assisted method was later repeated and improved by changing the template material or altering deposition method [36-38]. Another well-established technique for TNTA synthesis is hydrothermal method which is firstly explained by Kasuga *et al.* [39]. Hydrothermal synthesis is a solution-based method which involves in treating TiO_2 powders with NaOH aqueous solution. The as-obtained TiO_2 products are random-orientated and needle-shaped crystals with tube structure. Electrochemical anodization, another popular means by which we have obtained TNTs in our entire research process, was firstly conducted by Zwilling *et al.* in 1999 [40, 41]. According to their report, titanium and its alloy (Ti-6Al-4V) were anodized in chromic acid solution without or with the addition of hydrofluoric acid. Results indicated that

hydrofluoric acid was essential for the formation of porous films. The advantage of electrochemical anodization method over the other two is that the obtained nanotubes are self-aligned with high length-to-diameter ratio [42]. The widely accepted mechanisms of the aforementioned synthesis strategies as well as the morphology of as-obtained TiO_2 nanotubes from each of them are schematically shown in Figure 3 [36, 42, 43]. In terms of practical application, self-ordered nanotubes (Figure 3a,c) can provide straight forward pathway for charge carriers, which makes the charge transfer process more efficient on these nanotubes than on arbitrary-orientated TiO_2 nanotubes (Figure 3b). However, templated method is complicated and costly, and the tube morphology can be destroyed during the fabrication process [44]. Therefore, electrochemical anodization is chosen as a facile strategy for synthesizing nanotubes in our study.

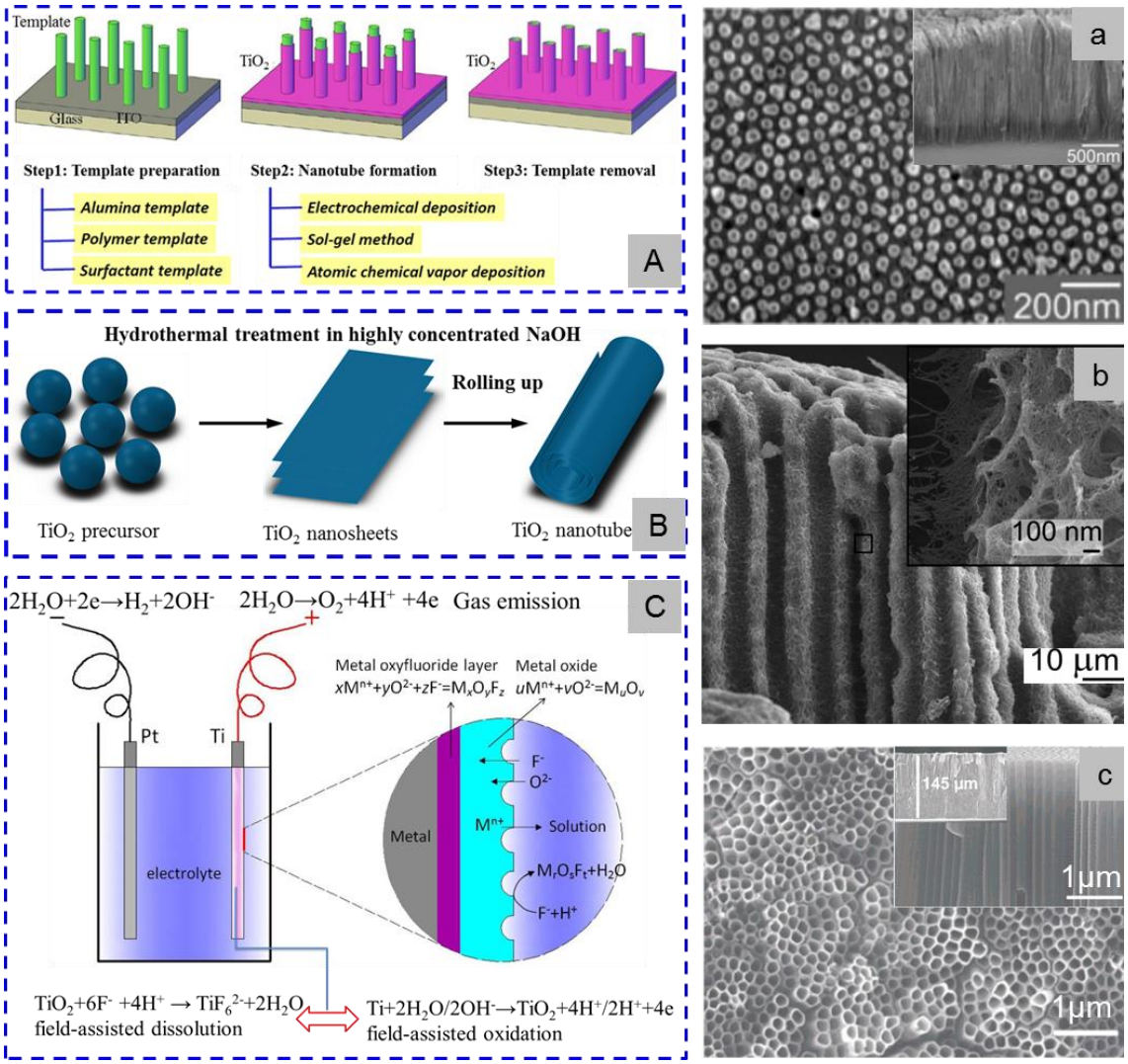

Figure 3 Mechanism of A. template-assisted, B. hydrothermal and C. electrochemical anodization synthesis methods [45]; morphology of as-prepared TiO2 nanotubes synthesized via a. template-assisted method [36], b. hydrothermal treatment [43] and c. electrochemical anodization [42].

1.2.3 Dimension control of TNTs

1.2.3.1 Length of nanotubes

The length of nanotubes can be easily controlled via varying the electrochemical anodization time. It is a crucial geometrical parameter that influences not only the active surface area, but also the e^-/h^+ pairs recombination rate [46]. In order to design an efficient TNTA photoelectrode, the nanotubes must be long enough to absorb all incident solar light, meaning that the tube-length has to be greater than the penetration length of the incident light. Meanwhile, as the majority carrier in n-type

semiconductors, photogenerated electrons have to travel along the nanotube from their generated sites to TNTs/Ti or TNTs/FTO interface in order to be further transported to the counter electrode. Those electrons which recombine with their counterpart holes before reaching the interface will thus not contribute to the photocurrent response. Thus, optimal length for the nanotubes should be the sum of light penetration length and electron diffusion length.

1.2.3.2 Thickness of tube walls

The thickness of tube walls is a parameter that requires delicate control of anodization time, voltage and even electrolyte composition. It influences overall PEC activity by restricting the behaviour of minority carriers, *i.e.* holes in TiO_2. In the tubular structure like TNTs, the charge carriers are always generated inside the tube walls, following by the vertical movement of electrons to the substrate and transversal movement of holes to the electrolyte. As a consequence, the path of the holes is always shorter than half the thickness of tube walls. At the interface of TNTs and electrolyte, a semiconductor/electrolyte junction is formed together with a depletion layer. Due to the significantly higher density of states (DOS) in the electrolyte compared to that in the semiconductor, the depletion layer builds up only in the semiconductor [47, 48]. Within the depletion region, the majority of carriers cannot stay, but will be driven to the opposite direction to minority carriers, realizing separation of e^-/h^+ pairs. The ideal situation will be that holes are generated inside the depletion layer so that charge carriers are efficiently separated.

1.2.3.3 Other parameters

There are other parameters of TNTA structures that can affect its PEC water splitting performance, such as periodicity of tube arrays [49], surface curvature [50] and additional surface hybrids (nanograss) [51]. The effect of these parameters can be referred to each reference article.

1.2.4 Limitations of TNTA as photoanode

Although the advantages of TNTA as photoanode are evident, there are some limitations that are worth noting. As shown in Figure 2, TiO_2 material has a BG ~ 3.2 eV. This means that it can only use ultraviolet (UV) light for photoactivation but is transparent to visible light and infrared light. This is unfavourable in terms of making the best use of incident photons because the latter two account for up to 95% of the solar light. As a result, shift of the absorption spectrum of TiO_2 material toward the longer wavelength region will make a great difference in the overall efficiency. Commonly applied strategies for this purpose are metal/non-metal doping [52-54], noble metal coupling/surface plasmonic resonance (SPR) effect [4-6] and narrow-banded semiconductor hybridization [55-57]. In addition, fast charge carrier recombination rate and relatively short charge carrier lifetime are also disadvantages that prevent TNTA-based PEC systems from making further breakthroughs.

1.3 Plasmonic effect

It is well established that modifications of either bulk TiO_2 or TNTA are necessary to increase its visible light absorption and make a high-performance photoanode. Among the commonly used modification strategies, ion doping of TiO_2 materials generates recombination centres and shortens carrier diffusion length, while semiconductor hybridization suffers from peeling off from TiO_2 surface and severe photon corrosion [6, 29]. On the contrast, loading noble metals on TiO2 provides a long-term stability and the ability to interactive with visible light [4, 6].

Surface plasmonic resonance is established when the oscillation frequency of electrons inside metal materials matches the frequency of incoming lights. The occurrence of SPR can result in scattering of incident photons of certain wavelength. The most commonly used metallic plasmonic generator for TiO_2 photoanode are Au and Ag nanostructures owing to the perfect match of their resonant photon wavelength with visible light spectrum [58]. A majority of researches have been carried out focusing mainly on incorporating Au/Ag of different morphologies into TiO_2 semiconductor

material in order to improve its ability to utilize visible light and separate e^-/h^+ pairs [4-6].

As schematically shown in Figure 4, there exist two theories with regard to the physics of SPR on enhancing the photocurrent response in a PEC process: (a) hot-electron injection theory [4] and (b) enhancement of local electromagnetic energy in the proximity of plasmonic nanostructures [5]. The former states that hot electrons at surface plasmon states are generated under the illumination of light at resonant wavelength. These electrons possess an increased negative energy level as compared to conduction band (CB) of the semiconductor photoelectrode, thus can be injected into the CB and consequently contribute to the photocurrent response. The second theory suggests that the enhancement of electric field intensity at the interface of plasmonic metallic nanostructure and semiconductor material (which can be up to 100×) can facilitate enormous e^-/h^+ pairs to be generated in the vicinity of the interface within the semiconductor. These charge carriers are ready to contribute to the enhancement of PEC efficiency due to their favourable near-surface sites.

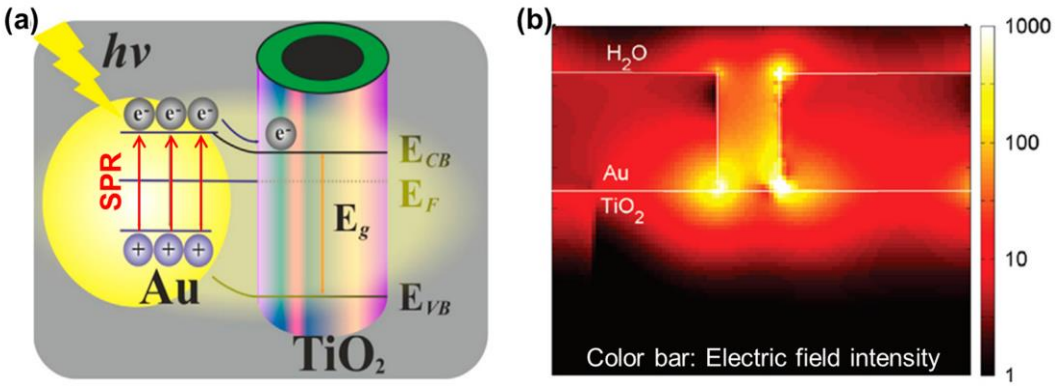

Figure 4 Principles of (a) hot-electron injection theory [4] and (b) enhancement of local electromagnetic energy in the proximity of plasmonic nanostructures [5].

1.4 Research focus

Although increasing the overall efficiency of PEC water splitting devices is the ultimate goal in terms of commercialization and industrialization, understanding the physics as well as discovering the best-performing material and modification strategy for

photoanode is the mean to reach the goal. In order to gain a deep insight into plasmon enhanced PEC water splitting on Au/TNTs systems, this PhD thesis has been developed from the background study of TNTA based PEC water splitting systems in the early stage (Journal paper 1), to the theoretical and experimental exploration on Au/TNTs system based PEC activities in the later period (Journal paper 2 & 3, Conference paper 3).

Au/TNTs photoelectrode has been proven promising in terms of improving both visible light utilization and charge carrier separation/transportation. However, insight into PEC enhancement mechanisms of Au/TNTs systems remains a short barrel and needs to be explored. My work thus focuses on the following three aspects:

PhD study topic 1: Gain an overview of recent advances of TiO_2 nanotube based PEC water splitting/hydrogen production.

A systematic knowledge on working principle of PEC water splitting and strategies to improve its performance is very important for further research activities in the relevant field. Therefore, efforts have been made to gain an overview of recent progress on hydrogen evolution through water splitting by using 1-D TNTs as photoelectrode materials. Morphology effects of TNTs, structures and compositions of photoelectrode materials are all found to be closely related to overall PEC efficiency and are thoroughly discussed in Journal paper 1.

PhD study topic 2: Fabrication and PEC performance of Au-TNTs photoanode.

Self-ordered TiO_2 nanotubes were synthesized via electrochemical anodization mentioned in section 1.2.2. Formation mechanism of anodized TiO_2 nanotubes was discussed in Conference paper 1. Au nanoparticles and nanoring structures were subsequently added to TNTs by magnetron sputtering technique (Conference paper 2 & Journal paper 3). In order to investigate photoelectrochemical properties of TNTs coated with different Au nanocrystallines, a series of electrochemical data of the test electrodes has been obtained and analysed, among which are photoconductivity measurement (Conference paper 3), I-V characteristic (Conference paper 2 & Journal

paper 3), transient photocurrent response (Conference paper 2 & Journal paper 3) and electrochemical impedance spectroscopy (EIS - Journal paper 3). Au nanoparticles and nanoring structures exhibit comparable performance with respect to enhancing photocurrent response. However, Au nanoring structure is more promising in terms of industrialization due to the fact that it is more controllable in dimension and periodicity (the SPR can thus be better defined).

PhD study topic 3: Numerical simulation as a method of investigating SPR effect on Au/TNTs systems.

Qualitative study of SPR effect is carried out on TiO_2 models loaded with gold nanoparticles / nanoring structures (Journal paper 3) via COMSOL Multiphysics modelling software. Finite element analysis is performed through electromagnetic wave module under frequency domain. Such numerical investigation provides distinct insight into the working mechanism and law of change of SPR effect. Meanwhile, Au nanodisk embedded TiO_2 nanohole arrays are proposed as a novel but promising structure which fulfils both the requirements of good photoactivity and precise control of plasmonic resonance (Journal paper 2).

1.5 Scope of current thesis work

The simulation work in this study emphasizes on utilization of numerical approach for exploring the physics of electrochemical water splitting as well as discovering new possible nanostructures for the process. Although we have suggested techniques for fabricating the Au nanodisk embedded TiO_2 nanohole arrays, the realization of such structure is outside the scope of the current thesis work.

2 Experimental setup

2.1 Electrochemical anodization of TiO_2 nanotubes

Self-ordered TiO_2 nanotube arrays were prepared by electrochemical anodization (Figure 5a). Ti foils (see Figure 5b) were connected to anodic side of the power source (DC-direct current, 50 V) after degreased and cleaned by sonication (Finn-Sonic M12) in acetone, isopropanol and deionized (DI) water for 5 mins each. Another metal electrode of the same size was positioned 3.5 cm apart from Ti foil and connected to the cathodic side of the power source. Two electrodes were physically fastened and immersed together into electrolyte consisting of 0.5 wt.% NH4F, 3 vol.% deionized H_2O and 97 vol.% ethylene glycol. In order to keep the anodization process within a homogenous electrolyte, a magnetic bead was used to stir the bath during reaction. Anodization time was controlled accordingly to get desired tube length. The as-prepared TNTs were then rinsed with ethanol in ultrasonic bath (BRANSOIC 3510E-MTH) and transferred to high temperature furnace at 450 ^oC for annealing to obtain anatase TiO_2. Appearance of annealed TNTA membrane attached to Ti foil is shown in Figure 5b (right).

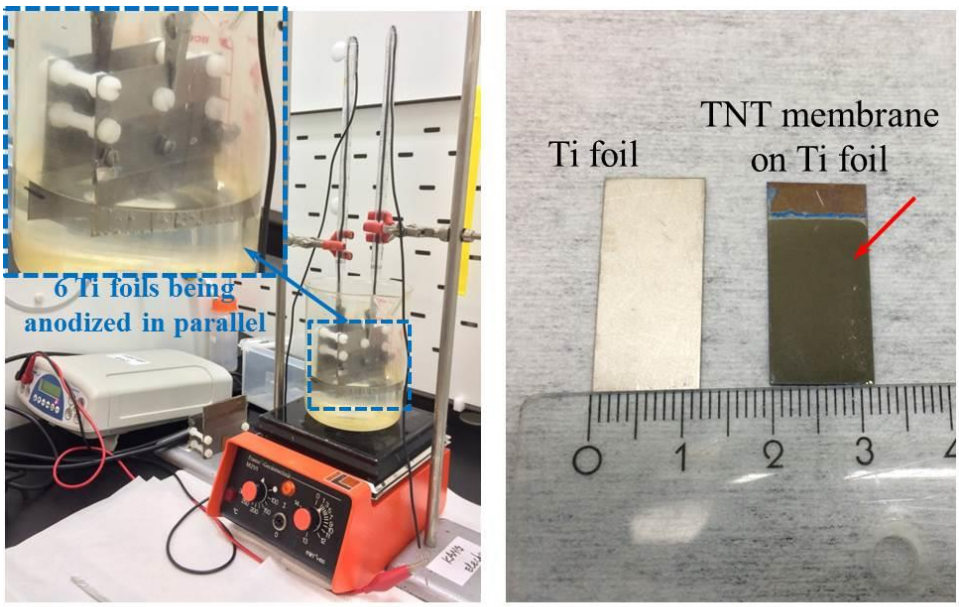

Figure 5 (a) Electroanodization of Ti in process; (b) Appearance of Ti foil and TNTA membrane on Ti.

2.2 Sputtering of Au nanoparticles and nanoring structures

Metallic gold was introduced to TNTA samples via magnetron sputtering (VG Microtech Polaron SC500 for samples used in Conference paper 3 and AJA International, Inc. for those used in Journal 3, shown in Figure 6a) with deposition time varying from 1 min to 3 minutes. The appearance of TNTA has changed from dark yellow for as-annealed TNTA, dark grey for 1-min sample to black for 2&3-min samples (Figure 6b).

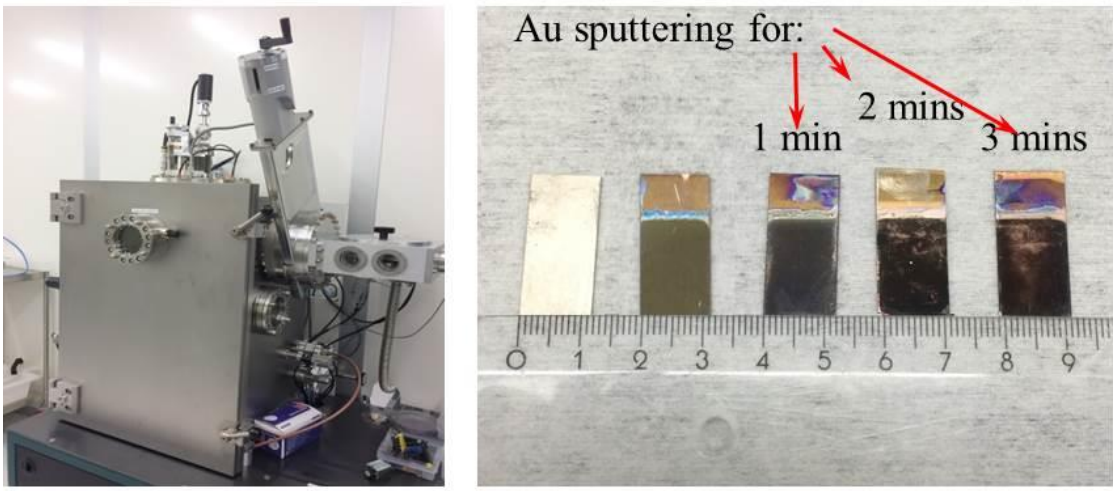

Figure 6 (a) AJA sputtering machine and (b) appearance of TNTs after gold sputtering for 1, 2 & 3 mins

2.3 PEC measurement

All photoelectrochemical and electrochemical measurements (I-V characteristic, time transient measurement and electrochemical impedance spectroscopy) were implemented using impedance measurement unit of Zahner elektrik IM6 electrochemical workstation (Figure 7a) and carried out in 0.5 M Na_2SO_4 solution in a standard three-electrode-configured quartz cell (PINE Research Instrumentation, Figure 7b). During all measurements, we set up (Au/)TNTs samples as working electrode, Ag/AgCl (saturated KCl filling solution) as reference electrode and a platinum wire as counter electrode. The samples (1 cm^2 in active area after sealed at

surround with opaque insulation tape) were illuminated by a 100 mW/cm^2 Schott KL1500 LCD light source.

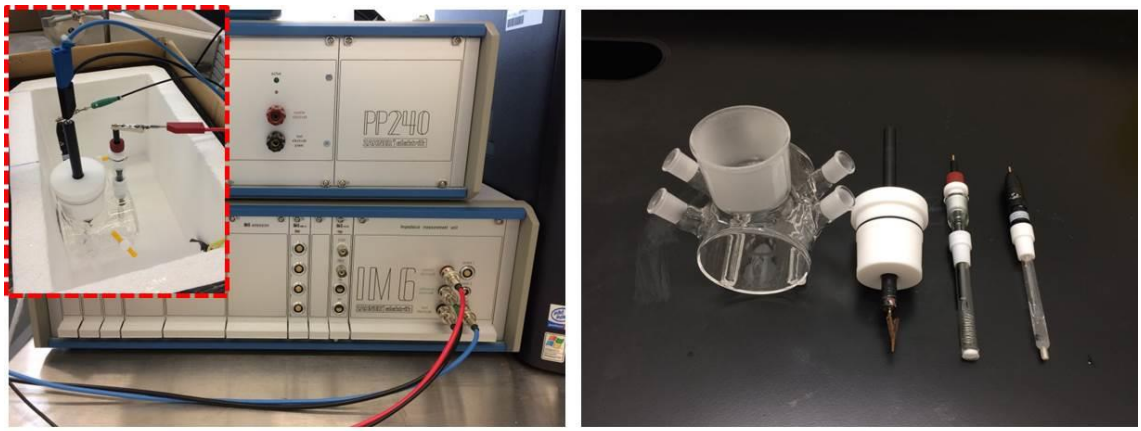

Figure 7 (a) Quartz reaction cell and (b) Zahner Elektrik impedance measurement unit. Inset: PEC measurement setup

2.4 Other characterization tools and methods

- Scanning Electron Microscope (SEM) – surface morphology characterization
- Energy-dispersive X-ray Spectroscopy (EDX) – element analysis
- X-ray Diffraction Analysis (XRD) – crystal structure analysis
- UV-VIS spectrophotometer - light absorption spectrum measurement

3 Summary of main research results

3.1 Preparation and characterization of (Au/)TiO_2 nanotubes

3.1.1 Study and fabrication of anodic TiO_2 nanotubes

3.1.1.1 Formation mechanism study

Even though anodic TNTs have been widely used for PEC water splitting/hydrogen evolution and other aspects, the formation mechanism remains unclear. While synthesizing and modifying anodic TNTs for PEC water splitting study, we have tried to further understand and investigate on how nanotubes are initiated and formed via FEA (Conference paper 2).

One of the most commonly accepted theories that can explain the initiation and formation process of anodic TNTs is call field-assisted dissolution (FAD), putting forward by O'Sullivan *et al.* [59] in 1970. FAD can be briefly described as the competition of field-assisted oxidation (FAO-Equation (1)) occurring at the metal/oxide interface and field-assisted dissolution (Equation (2)) which occurs at the oxide/electrolyte interface.

$$Ti + 2H_2O/2OH^- \rightarrow TiO_2 + 4H^+/2H^+ + 4e^- \quad (1)$$

$$TiO_2 + 6F^- + 4H^+ \rightarrow TiF_6^{2-} + 2H_2O \quad (2)$$

However, there have been theoretical limitations with regard to FAD model: 1. Dissolution reaction shown in Equation (2) can be difficult considering that H^+ in the electrolyte near the anode will be driven away under the effect of electric field; 2. Hemispheric tube bottom cannot be guaranteed because the electric field, which controls etching process at the bottom of the nanotube, tends to accumulate on the tip point and gives a sharp feature.

In order to clearly illustrate how the electrical field distributing on the working electrode, as well as to evaluate the influence of the existence of electrolyte on the etching process, dynamic simulation on electric domain of titanium anodization has been performed by COMSOL Multiphysics software. Arrows in Figure 8(a) show that electric field distribution in the compact TiO_2 layer (barrier layer). According to Equation (1), H^+ ions can be newly generated during FAO process beneath the bottom of the nanotubes. These ions can then migrate under the electric force to the oxide/electrolyte interface and participate in dissolution reaction.

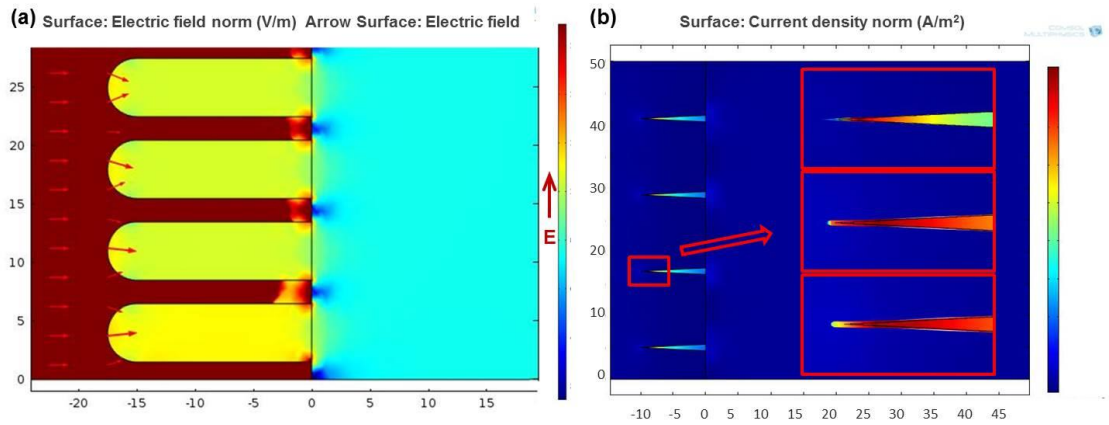

Figure 8 (a) Qualitative illustration of norm electric field beneath the bottom of nanotubes. (b) Shape-changing of the initial nanocracks overtime. Dimension of the geometry is shown in nm [60].

Figure 8(b) illustrates the initiation stage of the anodization process. This model is built based on nanocracks occurring on the surface of compact TiO_2 layer and offers a visual inspection on how the hemispheric bottom is formed. We performed a chemical process in an electric domain, which, as a result, requires a manually defined etching constant *K* and assign that the etching rate is the product of *K* and local current density. As is revealed in the figure, after a certain amount of time (which is dependent on the etching rate in the model and on the FEA reaction rate in practical), the cracks are both widened and lengthened. More remarkably, smooth bottom are formed gradually, and the maximum current density occurs on the neck of the crack instead of the tip.

3.1.1.2 Control of anodization parameters

There are several well-known rules with regard to controlling the dimension of TNTs during electrochemical anodization process, among which are that higher anodic voltage leads to larger diameters and longer anodic time results in longer tubes [3]. The importance of controlling tube length and wall thickness has been thoroughly stated in section 1.2.3. Wall thickness of nanotubes, according to Shankar *et al.* report [61], is related to the size of cations in the solution. Therefore, it is not a variant to consider in our study since we have been using electrolyte with the same composition in the entire study. As can be seen from the SEM images in Figure 9, the value of wall thickness is approximately equal to 8 nm in all cases. The tube length, on the other hand, is controlled to be around 15 µm for all the tested samples.

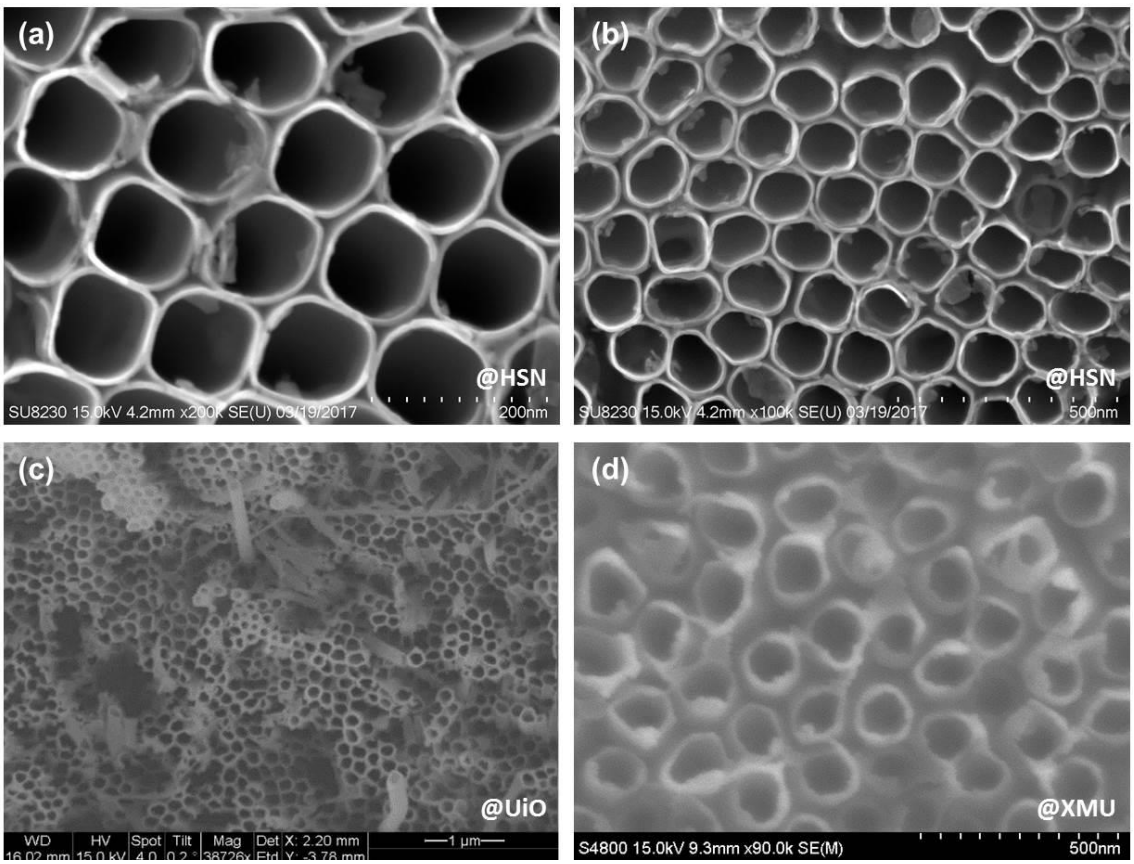

Figure 9 SEM images. Morphologies of nanotubes synthesized in (a,b) preserved or used solution and (c,d) new-made solution. (a,b) are taken at Høgskolen i Sørøst Norge (HSN) by FE-SEM, Hitachi SU 8230, (c) is taken at University of Oslo (UiO) by FEI Quanta FEG 600 and (d) is taken at Xiamen University (XMU)

As a matter of fact, according to Roy *et al.* [3], more precise control of the morphology and growing speed of TNTs also involves in controlling fluoride concentration and water content in the electrolyte. It is no easy job to control these parameters considering the fact that they vary from time to time during the whole anodization process due to ion consumption. As a result, it is practical to find a way for synthesizing a set of identical and meanwhile smooth nanotubes for subsequent modification and comparison.

It has been reported that organic solutions leads to smoother nanotubes than aqueous electrolytes due to much lower content of water [62]. During the experiment, we further found that nanotube walls synthesized in preserved or used solution (as are shown in Figure 9 a&b) are smoother and better aligned than those obtained from new-made solutions (as are shown in Figure 9 c&d). This is because that the water content in new-made solution is not steady in the ethylene glycol based electrolyte [3]. Ethylene glycol is hygroscopic and takes up water from environmental air, resulting in variation of water concentration [3]. In addition, nonuniform distribution of tube length and detachment of tubes from Ti substrate are observed on the sample in Figure 9(c), which can be attributed to the insufficient cleaning of substrate prior to anodization. Details will be mentioned in the following section.

In addition to smooth and good arranged nanotubes, it is also necessary that samples for modification should be highly identical in morphology and dimension to the pristine samples. Anodizing samples one by one cannot guarantee such identity considering the uncertainty of the electrolyte composition after preservation or first-time use. We thus apply a six-in-one clip (see inset in Figure 5a) where six Ti foils are clipped together and etched at the same environment. Figure 9 a&b are two of the six samples anodized using the six-in-one clip and exhibit high identity with regard to both tube dimensions and morphologies.

3.1.1.3 Pre- and Post- processes

As mentioned in section 2.1, all Ti foils were degreased and cleaned before anodization process. Application of contaminated Ti foils tends to resulting in large areas of cracks and detachment of TNTA membrane from Ti substrate. The significance of post cleaning, on the other hand, lies in the fact that it helps to remove the randomly distributed residual nanotubes (nano-grass) on the top openings of self-aligned nanotubes. The nano-grass has been proved to have negative effect on PEC performance [51]. Two SEM images under the same magnification and working conditions in Figure 10 allow us to visually compare nanotubes grown on Ti foils (a) without and (b) with pre- or/and post- cleaning.

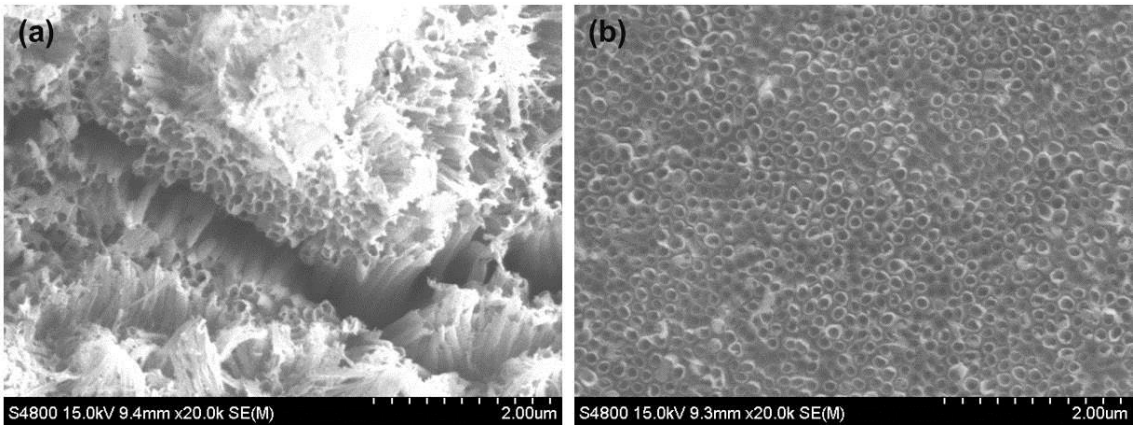

Figure 10 Morphologies of anodic TNTA (a) without and (b) with pre- and post- cleaning processes.

Generally, as-prepared TNTs are amorphous and can be converted to crystalline structure by thermal annealing. Compared to amorphous structure, crystalized TNTs exhibits enhanced electron mobility, lower electrical resistance as well as improved corrosion resistance and antibacterial activity [63-65]. XRD analysis (XRD @ UiO, AXS D8 Discover, Cu Kα radiation) in Figure 11 indicates that our as-prepared TNTAs are amorphous and show only diffraction peaks from Ti substrate. After annealing, crystallized TNTA is obtained with existence of pure TiO_2 anatase phase. The diffraction peaks at $2\theta = 25.28^{\circ}$, 37.80°, 48.05° and $53.89^{\circ}$are identified to be (101) (004) (200) and (105) crystal faces for anatase. ((004) face was mistaken for (112) in Conference paper 2).

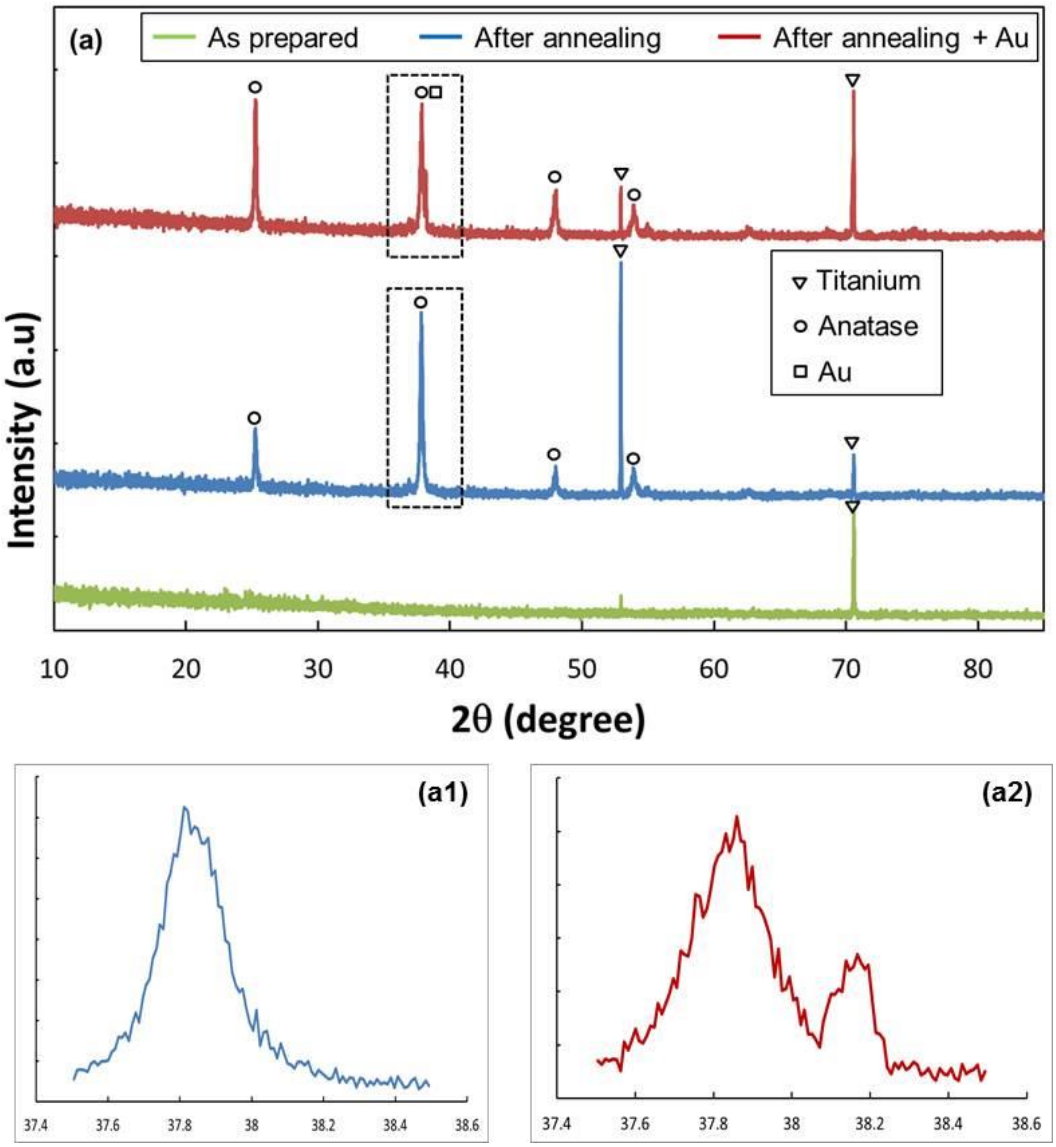

Figure 11 XRD pattern of amorphous and crystallized (Au/)TNTs/Ti. (a1) and (a2) are the enlarged details from the framed part in (a) [66]

3.1.2 Loading of Au nanoparticles on pristine TNTA

Different amount of Au nanoparticles can be loaded on crystallized TNTA by varying time during magnetron sputtering deposition. The existence of Au can be verified either by XRD and EDX analysis or from SEM/HRTEM images.

In Conference paper 2, XRD and EDX were utilized to demonstrate Au element on TNTA samples. Figure 11 has already shown the XRD pattern of Au/TNTs sample (red). Due to the very close diffraction angles for anatase (004) at 37.80º and Au (111) at

38.19º, it is difficult to tell Au peak from anatase peak. Figure 11(a1) and (a2) have revealed the detail information from 2θ = 37.5º to 2θ = 38.5º, and Au (111) peak can be observed in (a2). Besides, EDX characterization is also conducted for element analysis in Conference paper 2.

Alternatively, electron microscopy has been the main approach for morphology characterization and composition analysis in Journal paper 3. Morphology change of nanotubes can be observed from SEM images before and after accumulation of Au on the surface (Figure 12). Morphology of pristine TNTA is shown as comparison in Figure 12a. At sputtering time of 1 min (Figure 12b), granular Au crystalline grows on the mouth area of the TNTs with compact nanoparticle morphology. The thickness of tube walls changes to ~15 nm from original ~8 nm. When sputtering time increases to 2 mins, gold particles begin to merge on the top surface and thin nanoring structures start to form (Figure 12c). At sputtering time of 3 mins, smooth and thicker nanorings can be seen on top of the TNTs (Figure 12d).

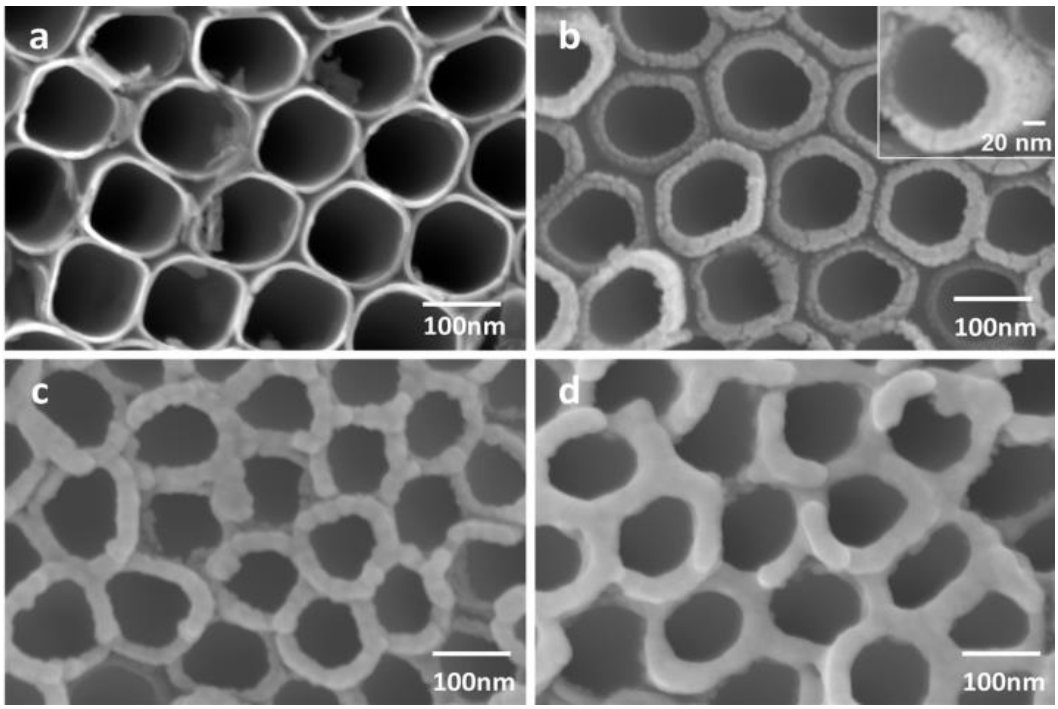

Figure 12 SEM characterization as a method to confirm the successful addition of Au via sputtering. Images are the top view of TNTA samples with a: 0 nm, b: 3 nm, c: 8 nm and d: 15 nm gold coating.

Figure 13 a-c show TEM images of Au distribution along single nanotubes corresponding to samples in Figure 12 b-d. It can be seen from the images that the quantity of Au nanoparticles decreases gradually from top to bottom. Larger accumulation can be observed near the top (opening) of nanotubes in b and c, which correlates to the top-view SEM images. Figure 13 e and f are HRTEM images of samples in Figure 13 a and b, with insets demonstrating their Fast Fourier Transform (FFT) from the selected area (I and/or II). Lattice spacing of 0.24 (and 0.236) nm and 0.2 nm can be observed from Au crystalline, which corresponds to the (111) and (200) lattice spacing, respectively. Well resolved lattice fringe of TiO_2 (400) (d=0.24 nm) is also observed in Figure 13e. Figure 13f is partial of a well preserved single nanoring structure (as shown in inset), thus no TiO_2 lattice is present. In addition, Au nanocrystallines on both samples exhibit FFTs where small spots make up rings. Therefore, the Au layer formed in our experiment is confirmed to be polynanocrystalline [67].

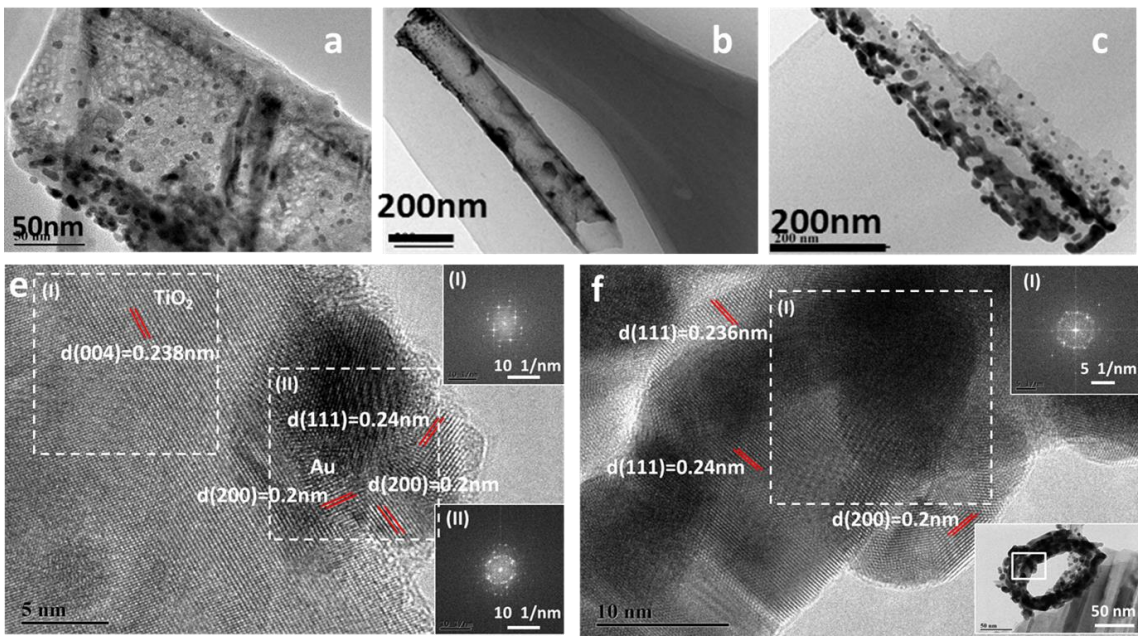

Figure 13 TEM images which show Au distribution on TNTs with a: 3 nm, b: 8 nm and c: 15nm Au coating. e and f are HRTEM images of samples in a and b. Insets in e are FFTs from selected areas and insets in f are FFT from selected area (top) and full view of a single nanoring structure (bottom).

3.1.3 Photoactivity

UV-visible light (UV-vis) spectrum is a straightforward way to examine photoresponse of the semiconducting material and identify the resonance wavelength of SPR effect. To this end, UV-VIS spectrophotometer (UV-2600) from SHIMADZU ($BaSO_4$ powder as reference) was used to measure the light absorption spectrum of target samples in the range of 220 ~ 850 nm, see Figure 14. The notations used in the figure indicate that the estimated thicknesses of Au layer on TNTA samples are 0 nm, 3 nm, 8 nm and 15 nm, which corresponds also to samples shown in Figure 12 and Figure 13. In addition to TNTA samples, the spectrum of a reference sample made of TiO_2 powder is also plotted in the figure for comparison. It is obvious that all four TNTA samples present relatively enhanced light absorption from 380 nm to 850 nm as compared to the reference sample. The enhancement is a result of the photonic properties induced from periodic arrangement of well-ordered TNTAs [49]. Comparing Au-loaded TNTA samples with pristine TNTA, the former exhibits higher absorption in the entire visible light region (380 ~ 850 nm) and absorption peaks can be found at certain wavelengths. The presence of absorption peaks confirms the occurrence of SPR effect on Au-loaded TNTs under visible light illumination. Among these samples, S_{3nm} shows a broadband resonance peak (500 ~ 650 nm). As gold nanostructure changes from nanoparticles to nanoring, the absorption peak narrows down and is blue-shifted to around 500 nm. According to Awang *et al.*'s report [68], SPR induced by gold nanograting can be shifted from ~550 nm down to ~540 nm when the gap distance is increased from 5 nm to 30 nm. Following this trend, it is understandable that our nanoring structure with average inner diameter of ~100 nm exhibits absorption peaks of around 500 nm.

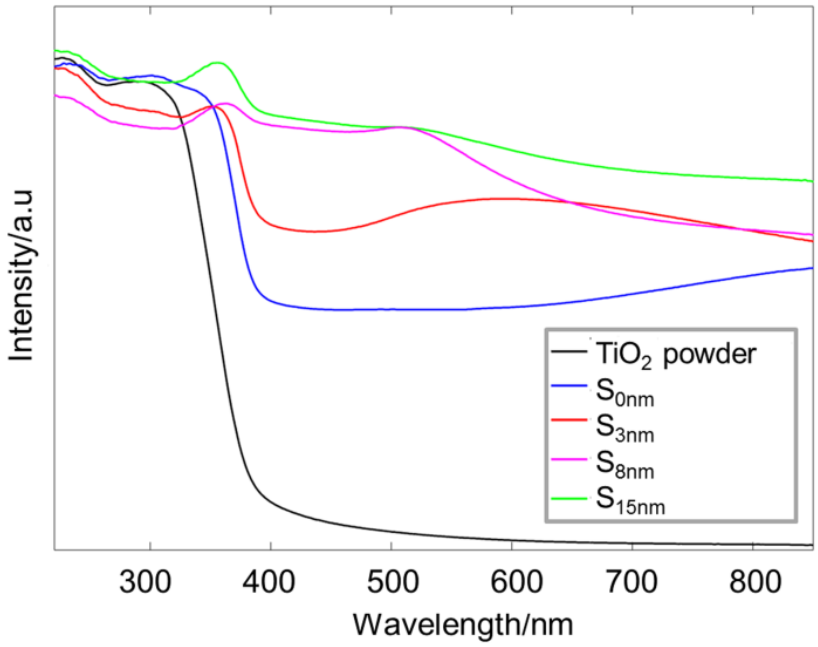

Figure 14 UV-vis absorption spectrum of TiO_2 powder and TNTA samples with Au layer of 0 nm, 3nm, 8nm and 15nm.

3.1.4 Current-Voltage (IV) characteristic

3.1.4.1 Photoelectric performance

Photoelectric measurement of Au/TNTs systems was first carried out in Conference paper 2 prior to PEC test. It is an easier approach than PEC measurement in terms of (1). gaining a basic idea on the photoelectric property and junction features of TNTs with and without Au and (2). predicting the potential mechanism of SPR effect.

Unlike PEC measurement where electrolyte is filled between anode and cathode, photoelectric measurement requires that ITO (or other metal cathode) is in direct contact with the top surface of the nanotube arrays. In the circumstance of PEC measurement, insulating tape or resin is always applied to the edges of the Ti/TNTs samples in order to avoid current leakage as well as to define photoactive area. However, due to the very thin layer of nanotube membrane, addition of insulating materials on top of the membrane will result in separation of TNTA and cathode, which subsequently leads to open circuit. Therefore, a setup without insulation (shown in Figure 15a) is used. Because of the existence of Schottky junction at the

semiconductor/metal interface, IV characteristic of pristine TNTA sample exhibits similar trend as a diode does under both dark and illumination conditions. The photocurrent response of pristine TNTA shows limited enhancement under sunlight but increases rapidly under UV illumination. On the contrast, owing to the conductive path formed (most likely) along the edges of membrane after sputtering of Au nanoparticles, the Au coated samples exhibit linear dependence of photocurrent on the applied voltage. See Figure 15b.

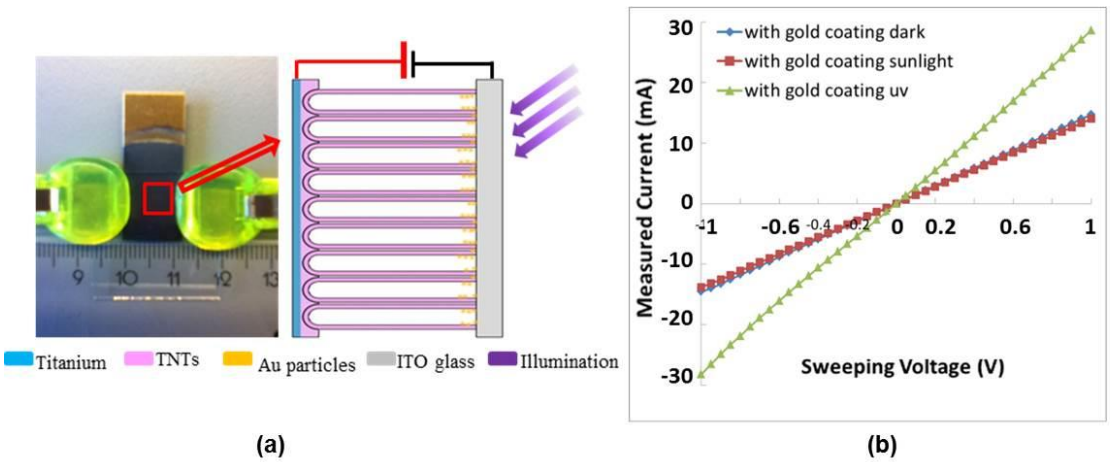

Figure 15 (a) Photo of the photoconductive measurement set up and schematic drawing of photoconductive measurement principle; (b) Conductive behaviour between current and applied voltage from Au-coated TNTA sample

Another significant discovery from photoelectric measurement is that no obvious SPR induced current enhancement is observed after Au coating. Such phenomenon can be explained by the enhancement of local electromagnetic energy in the proximity of plasmonic nanostructures (details have been described in Section 1.3). It is well-accepted that near-surface charge carriers are favourable during PEC process because of efficient separation of e^-/h^+ paris. The separation process can be described as follows: the new-generated near-surface holes are sufficiently captured through the oxidation reaction happening at the anode/electrolyte interface, leaving the electrons migrating to the back contact/cathode. This is one of the reasons that SPR improves the PEC efficiency by facilitating the generation of near-surface e^-/h^+ pairs. However, the case is different for a photoelectric process. Lacking of hole-consumer, near-surface electrons have higher chance to recombine with valence holes since it takes

longer for them to travel to back contact than for bulk electrons. If the length of nanotubes far exceeds the sum of light penetration length and electron diffusion length (as is mentioned in section 1.2.3), all near-surface e^-/h^+ pairs will recombine before any electrons reaching the back contact. The photocurrent response then remains unchanged as it is in Figure 14(b). On the other hand, should hot-electron injection dominate the SPR effect, there would be large amount of free electrons flowing through the system and the current would be rapidly enhanced.

3.1.4.2 Photoelectrochemical performance

IV characteristic is one of the most important features that can reflect the photo-to-current conversion efficiency of a PEC water splitting system. At a certain applied voltage, higher photocurrent response indicates better use of incoming photons and more efficient transfer of photo-generated charge carriers.

Figure 16 shows the IV characteristic of four identical TNTA samples coated with Au of varied morphologies: compact nanopartical (S_{3nm}), thin nanoring (S_{8nm}) and thick nanoring (S_{15nm}) under (a) dark and (b) white light illumination. Morphologies of four samples can be found in Figure 12. The contact between titanium substrate and TNTs is Ohmic in nature and Schottky contact exists only at the interface between TNTs and Au/electrolyte. As a result, all of the four samples behave analogically to diode under dark condition, *i.e.* current increases exponentially with increased forward bias but is nearly zero under reversed bias (Figure 16a). When illumination is applied on the samples, e^-/h^+ pairs will be generated within TiO_2 material. The electrons are then driven to the cathode for HER while holes participate in OER at the TiO_2/electrolyte interface. Photocurrent is formed through such opposite flow of e^-/h^+ pairs and can thus be measured as an indicator for PEC water splitting efficiency. It can be seen from Figure 16 (b) that additional Au on the TNTA can increase the photocurrent by over four times as compared to pristine TNTA. The enhancement is induced by increasing usage of incident light and efficient separation and transfer of charge carriers. Moreover, compact Au nanoparticle (S_{3nm}) exhibits the highest enhancement in

photocurrent among all three morphologies, and the current response is gradually decreased as the amount/thickness of the Au nanocrystalline increases.

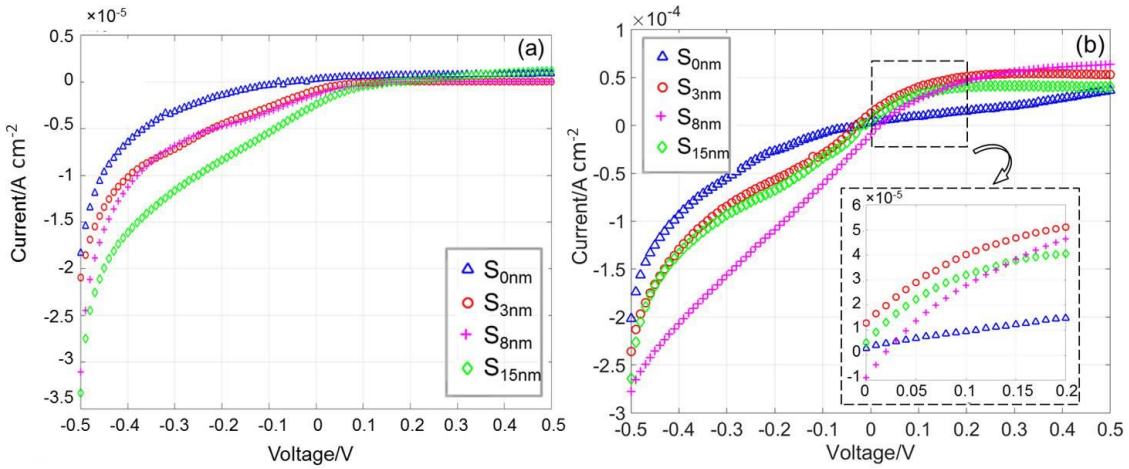

Figure 16 I-V characteristic of four samples under dark (a) and illumination (b) conditions. Inset in (b): magnification of voltage range from 0 to 0.2 V.

3.1.5 Time-transient performance

Time transient performance is a straightforward measurement to visualize the current enhancement induced via illumination. Meanwhile it reveals also how fast the samples can react to illumination and how long it takes for the samples to go back to original inactive state.

Figure 17 (a) shows the transient photocurrent response of different Au/TNTs samples during a PEC water splitting process at applied voltage of 0.2 V with white light illumination of intervals ON (20 s)/ OFF (40s). All the samples were kept under illumination for 10 s before recording started. It is observed that Au-nanoring-coated TNTA samples stabilizes at around 40 µA after 10 s pre-illumination, while Au-nanoparticle-coated sample keeps decreasing gradually after a ramp-up at the onset of illumination. Such decay behaviour has also reported by Liu *et al.* [5] where it was explained by the releasing of charge trapped at the TiO_2 surface upon irradiation. However, it cannot explain how the morphology of Au layer is related to this ramp-up behaviour. In the following Section 3.2.1.3, we will put forward a distinct theory based on a series of numerical simulation to explore the difference between SPR effect

generated by Au nanoparticles and nanoring structures. Nevertheless, current enhancement induced by adding Au nanoparticles is the highest during the whole light-on intervals despite of gradual decay.

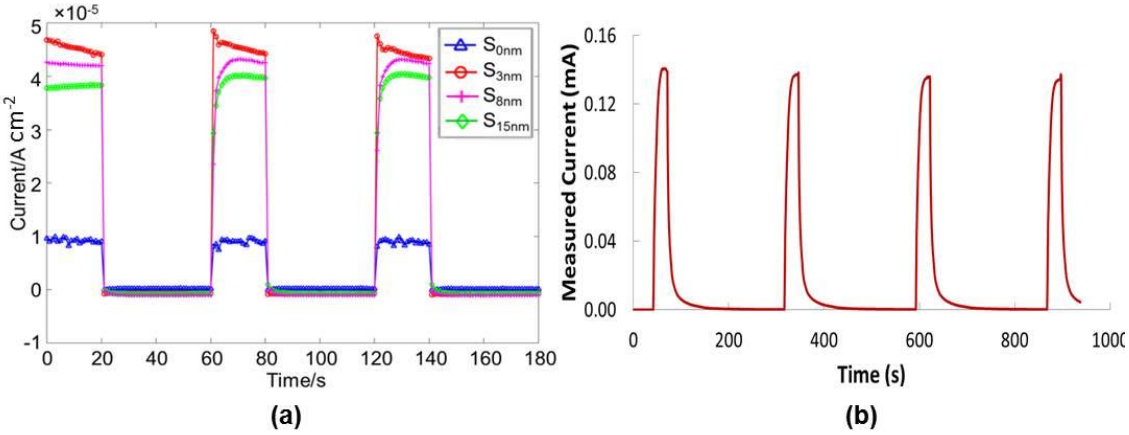

Figure 17 (a) Time transient measurement under white light illumination of Au-TNTs samples in a PEC water splitting process; (b) time transient measurement under UV illumination of a pristine TNTA sample for photoelectric property test.

Similar time transient study has also been done on other Au/TiO_2 nanostructures. In 2016, surface plasmon enhanced photocatalysis of Au/TiO_2 nanopillar arrays (TNPA) was carried out by Shuang et al. [69]. Besides the difference in base TiO_2 nanostructure (TNTA *vs.* TNPA), the distribution of Au nanoparticles in our current experiment is more compact than in ref.[69]. A comparison has been made between our pristine TNTA structure with their as well pristine TNPA in terms of photocurrent density. At half the bias voltage and illumination intensity of the latter, the former exhibits one order of magnitude higher current response than the latter. Such outstanding performance of TNTA can be largely originated from the increased surface area as compared to nanopillars. On top of that, the three TNTA samples with gold coating in our experiment present photocurrent of 4 to 5 times higher than that of bare TNTs upon irradiation, while Shuang *et al*. reported only 1.25 and 2 times enhancement after varied amount of Au deposition. We can thus suggest that the photocurrent response on TiO_2/Au-nanoparticle system can be enhanced by increasing the quantity of Au nanoparticles. This statement will be further proven by FEA study in Section 3.2.

Stability of the samples is tested by recording the photocurrent density for 10^4s under illumination. Data recording started 20s after illumination began. Figure 18(a) shows that S_{3nm} and S_{8nm} demonstrate stable photocurrent of approximately half the initial/maximum value after ~1000s, which indicates a 50% decrease from initial to stable state. Compared to these samples with relatively less quantity of Au coating, S_{15nm} exhibits less decay from initial ~38 μA cm^{-2} to stable ~24 μA cm^{-2}, corresponding to a 37% decrease. We have repeated the same measurement on these samples after one week (shown in Figure 18(b)) and gotten graphic curves with similar trends and values as in Figure 18(a). Such result indicates that the reduction of current density within the first 1000s in Figure 18(a) is not permanent, meaning no irreversible structure or morphology change on the samples. The less current decay in S_{15nm} can be attributed to more grain boundaries of the polycrystalline Au in the thick ring structure which provides more surface reacting sites and results in stable state of higher photocurrent. However, further research to identify the grain boundaries in polycrystalline Au of different morphology is needed regarding to this phenomenon.

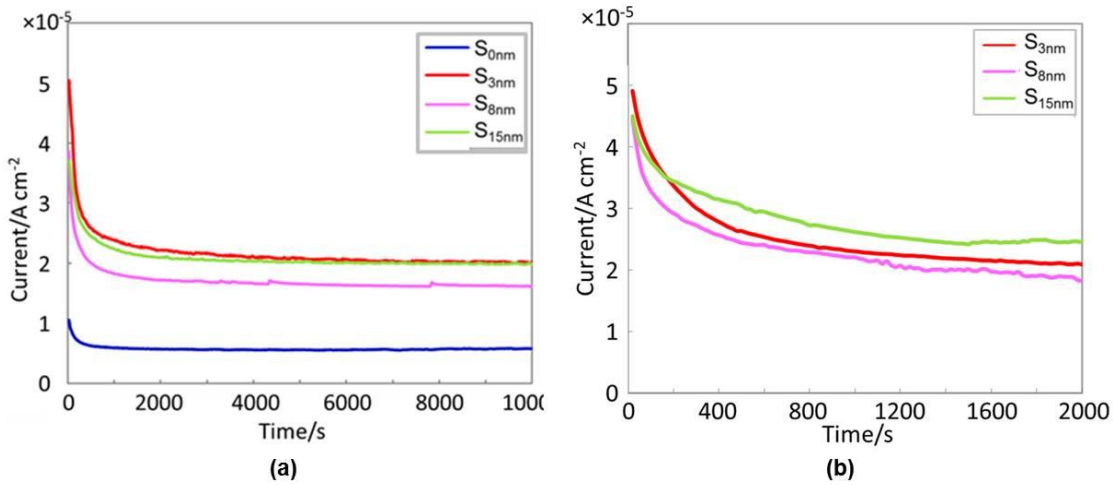

Figure 18 (a) Photocurrent stability of all samples for 10^4s; (b) Second time photocurrent stability test demonstrates a comparable result with (a) - Only data of the first 2000s are shown.

3.1.6 EIS measurement

Electrochemical impedance is the response of an electrochemical system to an applied potential. Unlike DC techniques and single frequency measurements, EIS is frequency

dependent and offers more information that helps to better understand the underlying interfacial problems and identify diffusion and capacitive behaviour of the system.

In order to reveal the PEC water splitting process happening at the surface of two electrodes, EIS under potentiostatic regulation has been conducted over frequency range of 10^{-2} - 10^{6} Hz (potential perturbation = 5 mV). Figure 19 is the Nyquist (a) and bode (b) plot of the EIS data acquired from different Au/TNTs systems under white light illumination. In the Nyquist plot in Figure 19(a), all samples exhibit two dispersion arcs on negative imaginary impedance plane (capacitive feature) and one arc on positive imaginary impedance plane (inductive feature). The inductive feature at the frequency region (> 10 kHz) is due to the measuring instruments and wire connections. The small arc occurring on each curve at the frequency region (0.1~10 kHz) is caused by the reactions happening at the counter electrode, and the large arc (0.01~100 Hz) is originated from the diffusion of electrons and charge transfer process on the working electrode. By comparing the circled curves (unfitted data) in four experiments, we find that S_{3nm} and S_{8nm} display more flat arcs than S_{0nm} and S_{15nm}, which is due to the rougher surface of the former samples as can be observed from Figure 12. Fitting of Nyquist data is done using the equivalent circuit model (ECM) shown in Figure 19(c), where the impedance of the constant phase element (CPE) and Warburg are defined as [70, 71]

$$Z_{CPE} = \frac{1}{Q * (j * 2\pi f)^{\tau}}$$

$$Z_{warburg} = \frac{Z_0}{(j * 2\pi f)^{0.5}} \tan(j * \tau * 2\pi f)^{0.5}$$

The fitting parameters indicate that the value of charge transfer resistance on the working electrode (denoted as $R_{ct,A}$) reaches minimum on S_{3nm} (1.21 kΩ) and S_{8nm} (1.03 kΩ), which is only ¼ of that on S_{0nm} (4.89 kΩ). This is consistent with the current response characteristic. The diffusion feature (which is normally indicated by a straight line in the low frequency region) does not obvious in the figure, suggesting that the

reaction is slow and these two process is overlapped but denominated mainly by chemical reaction in the low-frequency region. Apart from the transition region, fitting by the given ECM gives some mismatch in the low-frequency region (activities on the working electrode). The imperfect fitting for large arcs is mainly attributed to the dispersion of time constant (τ). The ECM is based on electrodes with flat and smooth surface where the interface of the electrode and electrolyte is continuous and even, *i.e.* time constant of CPE is an indeed constant. However, when using nanotubes as electrode, the roughness and porous feature of TNTs cause τ to be redistributed along directions both parallel and vertical to the surface, *i.e.* τ is rather a parameter that follows a specific distribution than a constant [71]. The fact that fitting on the Pt electrode, which has a smooth surface condition, is much better than on TNTA electrode verifies the statement above. In addition, Orazem *et al*. has also pointed out that large amplitude potential perturbation (above 1 mV) causes asymmetry of current density about zero and can lead to error in low-frequency impedance response [71].

Wang *et al.* indicates that the frequency where valley occurs in bode plot is the characteristic frequency (f_c) and its value is corresponded to the electron lifetime within working electrode [70]. It can be seen from Figure 19(b) that the f_c for four samples are $f_{c_0nm} \approx 0.3$Hz, $f_{c\_3nm} \approx f_{c\_8nm} \approx 0.8$ Hz and $f_{c\_15nm} \approx 0.5$ Hz, respectively. In our electrochemical system where electron/hole pairs are main current carriers, higher f_c values indicate that electrons are efficiently transferred away from working electrode to join chemical reaction and contribute to photocurrent response. Thus, the transferring speed of electrons within samples S_{3nm} and S_{8nm} is nearly 3 times as fast as the speed in S_{0nm} and nearly twice as fast as in S_{15nm}. We thus assume that a proper amount of gold, despite the difference in morphology, on TNTs contributes to optimization of the TNTs/electrolyte interface properties and accelerates the transfer of photo-generated electrons.

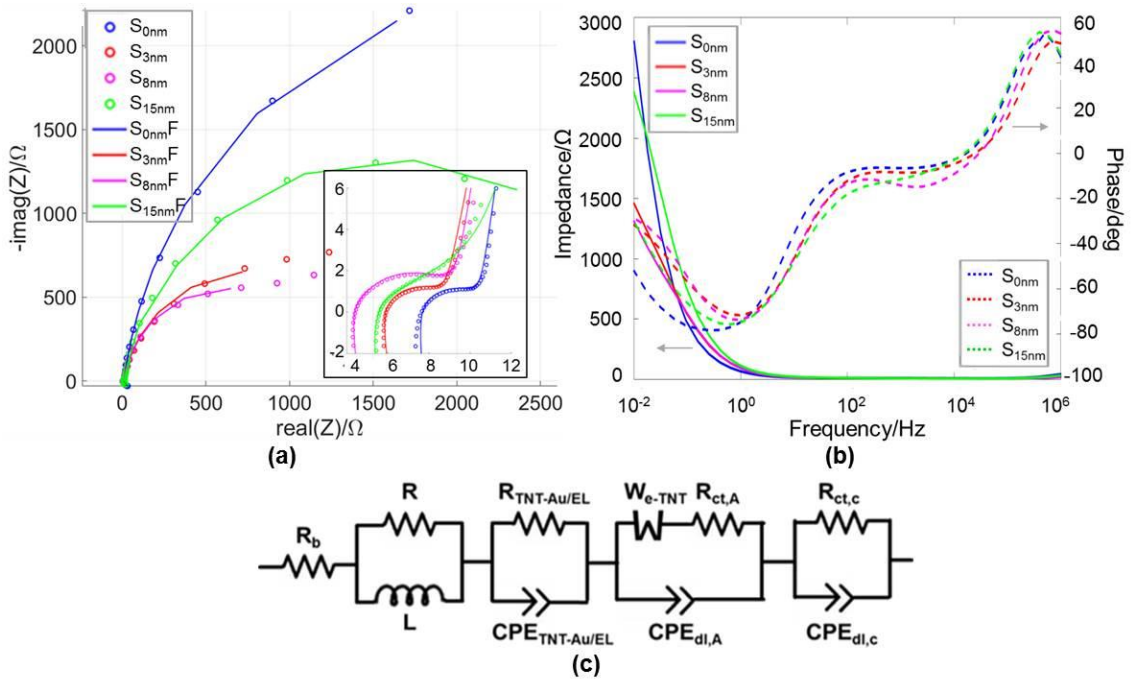

Figure 19 (a) Nyquist plot with fitting. Inset: details in high-frequency region; (b) bode plot: impedance (solid lines) and phase (dashed lines); (c) Equivalent circuit model for fitting Nyquist plot: R_b denotes the bulk resistance which includes resistance of electrolyte and connection wires, $R_{TNTA-Au/EL}$ and $CPE_{TNTA-Au/EL}$ in parallel model the diode feature at the interface of TNTA and gold (or electrolyte), $R_{ct,A}$ ($R_{ct,C}$) and $CPE_{dl,A}$ ($CPE_{dl,C}$) stand for the charge transfer resistance and double layer capacitance on the anode (cathode) respectively, Warburg element (W_{e-TNTA}) is used to describe the diffusion process of electrons in nanotubes.

3.2 Numerical investigation of SPR on Au/TiO_2 systems

It has been proven that loading of noble metallic nanoparticles to TiO_2 nanotubes can lead to surface plasmonic resonance, associating with the enhancement of an electromagnetic field in the vicinity of Au/TiO_2 interface. Numerical simulation with regard to SPR induced photoactivity on Au/TiO_2 systems is carried out in the study in order to: (1). understand the difference between SPR effect induced from Au nanostructures of different morphology and periodicity (Journal paper 3) and (2). discover industrialization-favourable Au/TiO_2 nanosystems whose dimension and SPR activity can be precisely defined (Journal paper 2).

3.2.1 Au nanocrystalline on TNTAs

3.2.1.1 Blue shift of SPR from Au- nanoparticle to nanoring structure

From optical absorption spectrum in Figure 14 we observed a blue shift from compact Au- nanoparticles (500 ~ 650 nm) to nanoring structures (~500 nm). In the following discussion, such blue shift is confirmed qualitatively via FEA through electromagnetic wave module under frequency domain. The agreement of experiment and simulation results, in turn, can demonstrate the validity of our numerical study.

Adapted from structure morphology shown in Figure 12, two 3D models of identical TiO_2 nanotubes coated with compact nanoparticles (M_{np}) and nanoring (M_{nr}) have been built (Figure 20). For simplify the shape of the Au nanoparticles, which can be whole or partial sphere, cylinder (nanorod) is used to model the particles. Liu *et al.* pointed out that the enhancement of local electric field (E) at the interface of TiO_2 and Au is proportional to the photon absorption [5]. As a result, the surface-maximum of the electric field intensity ($E_{s\text{-}max}$) on the top surface of TNTA has been used as the equivalent of the SPR effect. It has been observed that for Au layer with height of 5 nm, M_{np} exhibits $E_{s\text{-}max}$ = 2.8E10 V/m at λ = 800 nm, while the value of $E_{s\text{-}max}$ for M_{nr} is only 1/10 of the former which occurs at λ = 600 nm. SPR wavelength blue-shifts by ~200 nm from M_{np} to M_{nr}. The quantitative mismatch between simulation and experiment results from the model assumption and the adaption of refractive index from bulk TiO_2 material rather than an actually periodic nanotube structure. By varying the thickness of the Au nanoring structure in M_{nr} model, $E_{s\text{-}max}$ is found to occur at λ = 650 nm for thickness of 3 nm and remain at λ = 600 nm for thickness of 4 nm and up (up to 10 nm). The result agrees with the overlapping peaks of S_{8nm} and S_{15nm} in the absorption spectrum in Figure 14. By 2D plotting of electric field distribution on the top surface of nanotubes, we have further observed that the electric field distributes more uniformly and spreads deeper into the nanotube walls on M_{nr} than that on M_{np}. In fact, if the maximum surface average of the electric field ($E_{s\text{-}avg}$) is used instead of E_{max} to identify SPR wavelength, it is at λ = 750 nm where SPR occurs in M_{np} model rather than 800 nm as is mentioned earlier (where E_{max} occurs).

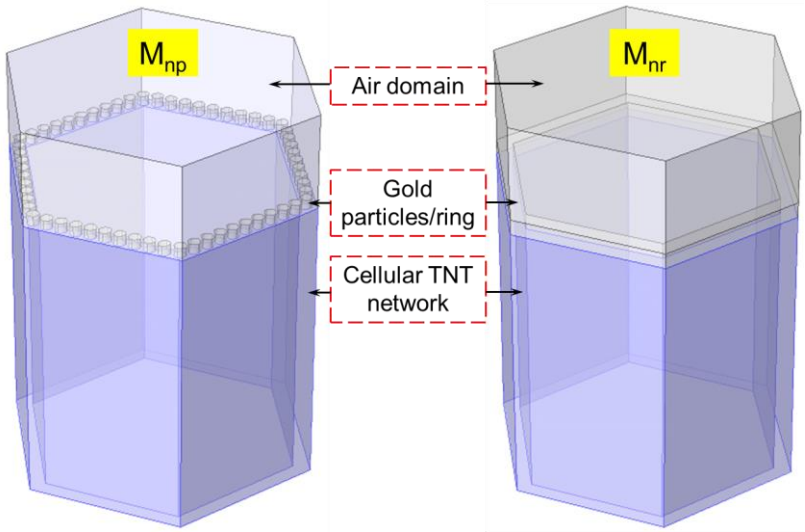

Figure 20 Numerical models of TNTA unit cell with compact Au nanoparticles (M_{np}) and nanoring structure (M_{nr}) on top

3.2.1.2 Other factors influencing SPR effect

Further simulation has revealed that there are other factors that can change the SPR wavelength and affect the intensity of near-surface electric field. Table II lists the SPR wavelength and corresponding $E_{s\text{-}avg}$ with regard to morphology and size/thickness of the Au layer. Several factors are found to be related to SPR in the following ways:

- For the same size of nanoparticles (group c *vs.* d and e), higher amount leads to larger $E_{s\text{-}avg}$ and red-shift of the resonant wavelength;
- For the same quantity of Au particles (group c *vs*. f), larger particle size gives higher $E_{s\text{-}avg}$ value and red shifts the SPR wavelength;
- For the same total contact-area between Au and TiO_2 (groups d and e *vs.* f), smaller particles of higher quantity exhibits larger $E_{s\text{-}avg}$;
- High uniformity can help to enhance the electric field intensity in the vicinity of Au/TiO_2 interface.

Considering the dimension limitation of a real whole or partial sphere, the height of the cylindrical structure used in the model cannot be larger than its diameter (indicated by NA - Not Applicable in the table). It is obvious that SPR changes following the variation of ratio between height and diameter of the modelled Au nanorod. Such

phenomenon suggests that when loading Au nanoparticles to TiO_2 (or other semiconductors), different contact angles will lead to changes of SPR in terms of both strength and position. However, it is almost impossible for all nanoparticles to keep identical contact angles, which explains the wide band absorption spectrum in Figure 14 and ref. [72].

Table II Plasmonic resonant wavelength with regard to morphology and size/thickness of the Au nanostructure[a]

Au thickness (nm)		2	3	4	5	6	7	8
Nanoring structure		700 (7.5e8)	650 (1.1e9)	600 (4.4e8)	600 (6.3e8)	600 (5.2e8)	600 (4.1e8)	600 (3.5e8)
Nano-particles[b]	Compact [c]	750 (3.8e9)	800 (1.4e9)	750 (1.8e9)	750 (1.8e9)	700 (2.7e9)	NA	NA
	Loose + uniform [d]	700 (9.4e8)	750 (8.5e8)	700 (7.7e8)	700 (7.3e8)	650 (8.3e8)	NA	NA
	Loose + nonuniform [e]	700 (6.3e8)	750 (6.2e8)	750 (6.8e8)	700 (6.3e8)	650 (7.7e8)	NA	NA
	Uniform + small [f]	700 (7.8e8)	750 (9.7e8)	750 (8.4e8)	NA	NA	NA	NA

[a] number without parentheses is the wavelength (unit: nm) where SPR occurs; number with parentheses is the electric field intensity at corresponding wavelength (unit: V/m).

[b] different size, amount and distribution of gold nanoparticles are considered: size of particles in *c, d,* and *e* are identical and larger than the size of *f*; amount of particles in *c* and *f* are equal, which is twice as much as that of *d* and *e*; the contact area of gold and TiO_2 in *d*, *e* and *f* are the same, which is half the value in *c*.

3.2.1.3 SPR effect in the vicinity of Au/TiO_2 interface

It is commonly accepted that generation of near-surface charge carriers is more favourable than bulk-level carriers in terms of creating photocurrent response as well as improving PEC performance. Therefore, it is necessary to investigate the electric field distribution in the vicinity of Au/TiO_2 interface the difference between nanoparticle- and nanoring- generated SPR effect will be presented. To this end, the following four models are built: M_{np_3nm} – TNT with gold nanoparticles of 3 nm in particle height, M_{np_5nm} – TNT with gold nanoparticles of 5 nm in particle height, M_{nr_5nm} - TNT with gold nanoring of 5 nm in thickness and M_{nr_8nm} - TNT with gold

nanoring of 8 nm in thickness. Subsequently, a series of cut planes (a typical cross-section plot in COMSOL where planes are created through a 3D in a 2D geometry to visualize a quantity as a family of plots) are created below the top surface of each TNTA unit cell, ranging from 1 nm to 10 nm apart from the top surface. $E_{s\text{-}avg}$ on these cut planes is then calculated so that the effect of SPR effect in the vicinity of TNTA top surface can be analysed. It is worth noting that the highest $E_{s\text{-}avg}$ value occurs at different wavelength for each of the three aforementioned models.

Figure 21 shows a series of surface plots of electric field distribution on the cut planes which are 2 nm (CP_{2nm}), 4 nm (CP_{4nm}) and 6 nm (CP_{6nm}) below the TNTA top surface on M_{np_5nm} and M_{nr_5nm}. As is already mentioned in 3.2.1.1, the colour distribution, *i.e.* distribution of the intensity of electric field is generally more uniform at all three surfaces on M_{nr_5nm}. It is especially obvious when comparing CP_{4nm} and CP_{6nm} in nanoparticle and nanoring models in Figure 21 that SPR induced enhancement in electric field intensity spreads deeper on M_{nr} than on M_{np}. Moreover, although the incident wave has the same polarization, the location of the maximum and minimum electric field intensity on nanoparticle and nanoring models is distinct. For nanotube coated with nanoparticles, the nanotube walls that are perpendicular to incident electric wave experience the minimum enhancement of electric field intensity. On the contrary, the same nanotube walls on M_{nr} demonstrate the strongest enhancement of electric field under the same polarization for incident electric field.

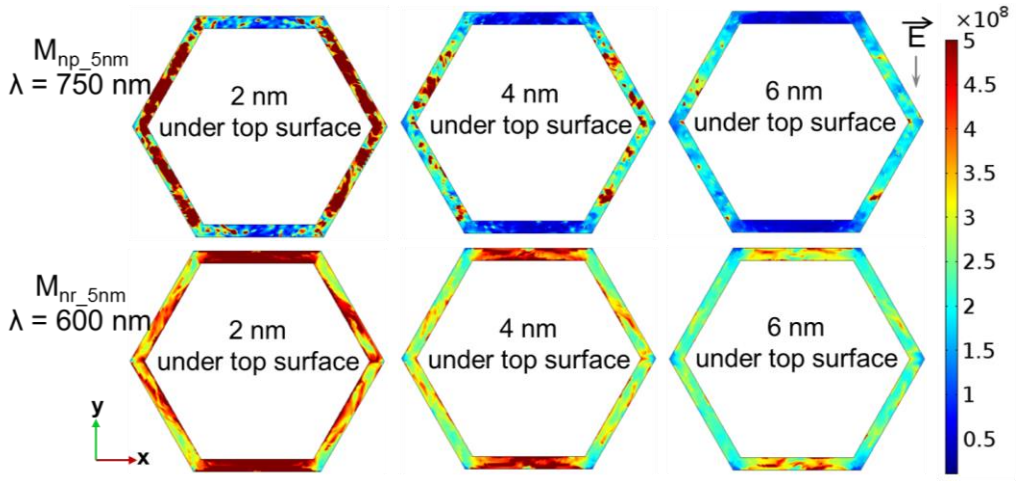

Figure 21 Intensity of electric field distribution on the cut planes which are 2 nm, 4 nm and 6 nm under TNTA top surface

Figure 22 is a plot of $E_{s\text{-}avg}$ on each cut plane versus the distance of the planes from the top surface on all three models. Interestingly, the curves in Figure 22 show similar trend as the transient current upon illumination (time transient response from 60 s to 80 s for S_{3nm}, S_{8nm} and S_{15nm} in Figure 17a are replotted as inset in Figure 22). The highest $E_{s\text{-}avg}$ locates on the Au/TiO2 interface for nanoparticles, whereas below and near the Au/TiO_2 interface for nanostructure. This is also true even for the same thickness of different morphologies (M_{np_5nm} and M_{nr_5nm}). As we all know that transient current is the process where current changes from one steady state to another. The cause for such change in Figure 17a is illumination. Under dark state, there are very limited charge carriers generated in the semiconductor, which restricts the current within a near-zero level. Under steady irradiation, the number of newly generated charge carriers and those recombine during bulk transportation reaches an equilibrium, which keeps the current in a certain value. At the onset of illumination, the sudden increase of electric field at the near-surface of TiO_2 boosts the generation of a majority number of local e^-/h^+ pairs. Comparing the coordinates used in these two figures, we can easily relate the current density to the amount of charge carriers generated under the enhanced electric field. While charge carriers drift to the back contact or electrolyte, there are several competing activities taking place at the same time, such as the scattering and reabsorption of incident photons, trapping of electrons, recombination and re-stimulation and *etc.*. Therefore, the generation sites

of the charge carriers can affect the ramping up behaviour by defining the travelling path of the charges. As a result, we correlate the two curves in Figure 22 and suggest that the instant current response upon illumination might be related to how the electric field is distributed and how the charge carriers travel and recombines along the longitudinal dimension of the TiO_2 layer.

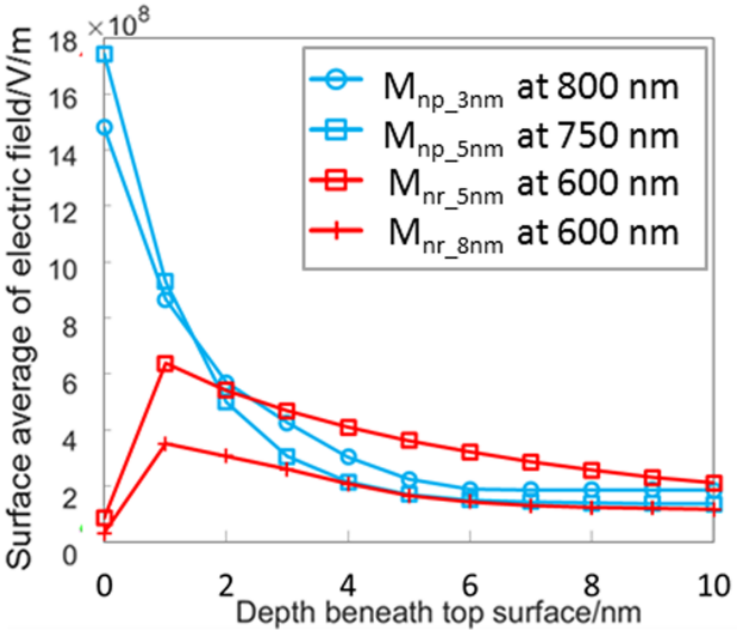

Figure 22 Dependence of $E_{s\text{-}avg}$ versus position of cut planes where $E_{s\text{-}avg}$ is calculated. Each $E_{s\text{-}avg}$ is calculated at the resonant frequency of each model.

3.2.2 Au nanodisk embedded in TiO_2 nanohole arrays

The most commonly investigated metallic structures for SPR generation are nanoparticles, nanocubes, nanorods and core-shells [5, 72-75]. However, direct placement of particles on 1D TiO_2 either by physical evaporation [5] or by chemical synthesis [4, 6] results in randomly arranged clusters on top of the functioning material, which is not desirable for a MEMS/NEMS fabrication process where precise control of the structure is required [76]. Another classic and more industrialized metallic SPR generator is nanograting. It has been widely applied to silicon-based solar cells and photovoltaic devices for the purpose of increasing photon absorption efficiency and reducing the required thickness of Si thin film [77, 78]. With properly

chosen periodicity and filling material in the grating slits, the SPR wavelength can be modified based on the equation below [79]

$$\frac{2\pi}{P} = \frac{2\pi}{\lambda}\left(\frac{\varepsilon_1\varepsilon_2}{\varepsilon_1+\varepsilon_2}\right)^{\frac{1}{2}} \quad (3)$$

where ε_1 and ε_2 are dielectric constants of the metal and slit filling material, λ is the resonance wavelength and P is the periodicity of the grating structure.

A conventional way to utilize a nanograting structure is to locate it on top of the functioning semiconductor materials [80, 81], but such approach results in blocking certain portion of incident solar photons. Furthermore, commonly used nanograting structures are polarization-dependent (sensitive only to TM-transverse magnetic modes) and additional filling material is always required in order for SPR to occur within the desired visible or infrared light region [77]. Therefore, we have proposed a novel optical structure where Au nanodisks are embedded in titanium dioxide nanohole arrays. The pattern and periodicity of such structure can be very well controlled and the integration does not have extra slit-filling material involved. The optical absorption features of the proposed structure are thoroughly studied via simulation in Journal paper 2.

The relative permittivity (ε) of TiO_2 in the visible light region is between 6 and 8. According to Equation (3), TiO_2 itself can be the perfect filling material for Au grating slits. For a periodicity ranging from ~150 nm to ~350 nm, the corresponding resonance wavelength will be 650 - 850 nm. Scheme of the proposed square-arranged nanohole structure is shown in Figure 23 where a single unit cell is red-highlighted. The notations used in the figure are as follows: P is the periodicity of the array (the same P as in the Equation (3)), t and d are the thickness and diameter of the filling Au layer, respectively, h is the depth of the holes (H=h-t) and T is the thickness of the Au back contact which is fixed at 50 nm. Making an analogy to electrochemically anodized nanotubes (Figure 12), the d is inner diameter of the tube which is around (P-30) nm

(30 nm is the double of wall thickness). In addition, an air domain of 100 nm (not shown in the figure) is also defined on top of the cell.

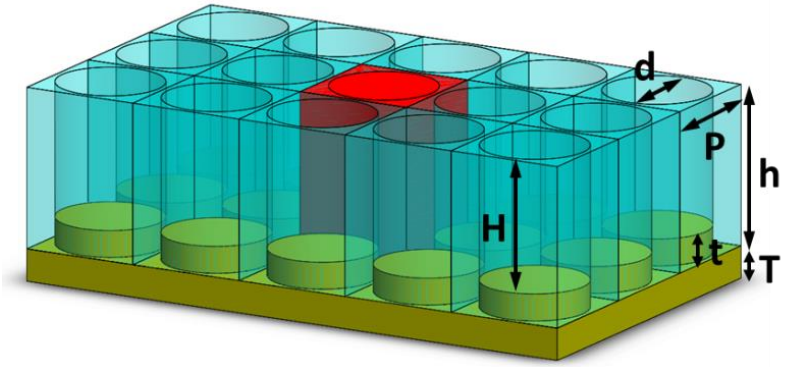

Figure 23 Scheme and dimension notations of the proposed plasmon-enhanced nanohole structure

Dispersive refractive indices of TiO_2 and Au used in simulation are adopted from [82, 83]. Different from bulk TiO_2 material, 1D TiO_2 nanostructure is not completely transparent to visible light (whose wavelength is beyond the band gap of TiO_2) due to its photonic properties and sometimes existence of defects, as can be seen from Figure 14. Hence, the simulation is implemented in the wavelength range of 300 - 950 nm, which covers the whole visible light region. As is reported by Han *et al.* [84], the absorption for nanohole array drops rapidly when the filling fraction exceeds 0.45. Consequently after calculation, we employ a periodicity (P) sweeping up from 200 nm. For boundary conditions, periodic condition and perfectly matching layers (PML) were applied respectively to side and bottom boundaries.

The absorption in the TiO_2 layer for a normally incident plane wave were calculated by [80]

$$\omega \cdot Im(\varepsilon) \int_V |E|^2 \, dV \tag{4}$$

where E is the local electric field and V is the volume of the TiO_2 nanostructure. Since the imaginary part of refractive index (Im(ε)) is largely dependent on periodicity and defects of 1D TiO_2 nanostructure, absolute value of the absorption calculated from adopted ε values from bulk TiO_2 cannot reveal the real case of our nanohole structure.

Therefore, the absorption enhancement factor (AEF) is introduced and defined as the ratio of absorption in the TiO_2 layer with and without Au disk fillings.

The effect of t (thickness of Au nanodisks) is first investigated with h = 150 nm. Simulation was initiated with normal electromagnetic (EM) wave incidence under TM modes and swept P (periodicity) and λ (wavelength) within the range of 240 - 360 nm and 300 - 950 nm, respectively. Results show no particular waveguide mode or SPR excited under wavelength of 400 nm. Coupling into TiO_2 waveguide mode occurs when λ increases to around 400 nm and the strongest coupling is reached at λ = 650 nm for all P values without Au fillings. There is no sign of distinct coupling mode caused by adding Au into the holes. However, due to the addition of Au layer, the actual depth of hollow area, H, is reduced, which leads to a different coupling factor. For example, the strongest coupling shifts from λ = 650 nm to λ = 600 nm when H is decreased from 150 nm to 100 nm.

Figure 24 shows the mapping of AEF with respect to incident wavelength and periodicity for (a) t = 50 nm, (b) t = 25 nm and (c) t = 10 nm. In Figure 24(a), a maximum AEF of 7 can be observed at λ = 750 nm due to the SPR effect. It can be observed that the resonant frequency is red shifted from 700 nm to 800 nm as the periodicity increases from 240 nm to 360 nm. Compared to experimental results where Au nanoparticles are randomly distributed on TiO_2 nanostructures (SPR = 500 - 600 nm) [4-6], the proposed structure gives a red-shifted SPR (> 700 nm). This can be explained by the larger lateral dimension of Au compared to the Au particles/clusters formed in the experiments [58]. Compared to the case when t = 50 nm, both Figure 24(b) with t = 25 nm and Figure 24(c) with t = 10 nm exhibit strong absorption enhancement at certain wavelengths which is not affected by periodicity. Especially, a broad and continuous absorption band from 700 nm to 850 nm is observed at t = 25 nm. By analysing the electric field distribution, we find different origins for the two peaks in Figure 24(b) (λ = 700 nm and λ = 800 nm). When λ = 700 nm both SPR effect and coupling mode are visible on TiO_2 nanohole arrays. However, in the case of λ = 800

nm, the coupling mode vanishes after inserting Au disks, leaving only SPR contributing to AEF.

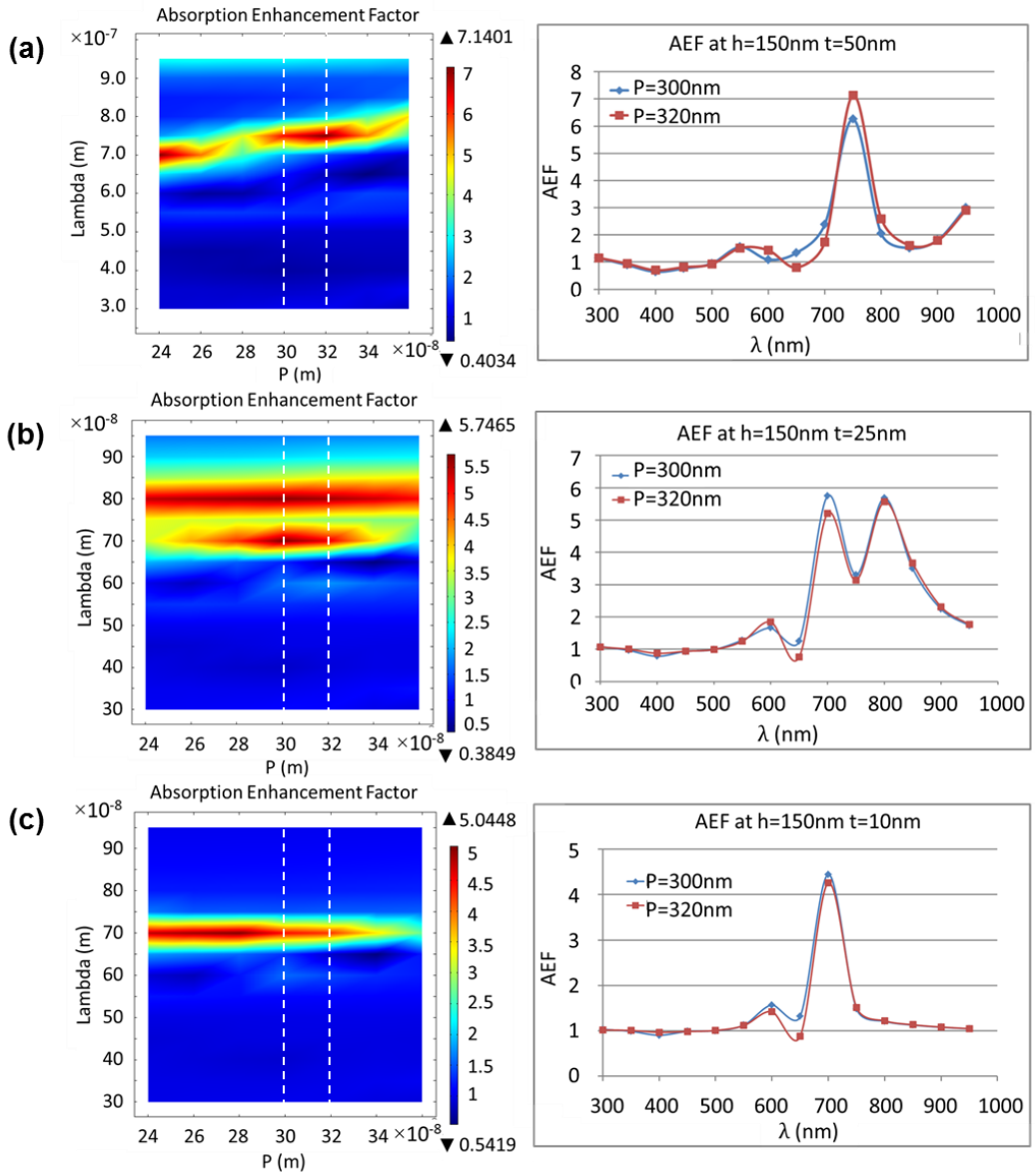

Figure 24 Mapping (left) and replotting (right) of absorption enhancement factor with respect to periodicity and incident wavelength for (a) t = 50 nm, (b) t = 25 nm and (c) t = 10 nm.

There are other phenomena that are worth noting in Figure 23. Absorption is found to be decreased at around λ = 400 nm and λ = 650 nm in all three circumstances. The decrease feature at λ = 400 nm is independent of periodicity, which can be attributed to light absorption on Au nanostructure of low aspect ratio [85]. This can also be proven by the fact that when t changes from Figure 24 (a) to (c), the absorption

decrease at λ = 400 nm is less and less remarkable. This is to say that the absorption of Au has been shifted out of the simulated wavelength region due to the change of aspect ratio of Au. On the contrary, the decrease in AEF at around λ = 650 nm occurs only for certain P values. Such periodic change in absorption behaviour at λ = 650 nm is largely attributed to the corresponding change of coupling mode with P value. Figure 25 graphically demonstrates how the coupling mode can be affected by the dimensions (P and H) of the nanohole arrays. At P = 300 nm (Figure 25a), the electric field is less influenced by the variation of H from 100 nm to 150 nm. However, when P increases to 340 nm, the change in H leads to obvious change in E distribution (Figure 25b): E couples mainly into TiO_2 domain for large H (H = 150 nm), but gets weaker and redistributes into the air domain as H decreases to 100 nm. At λ = 650 nm and P = 340 nm, the enhancement of electric field by SPR is not sufficient to compensate the decrease due to the recoupling in waveguide mode. Thus, the total absorption in the corresponding region is reduced.

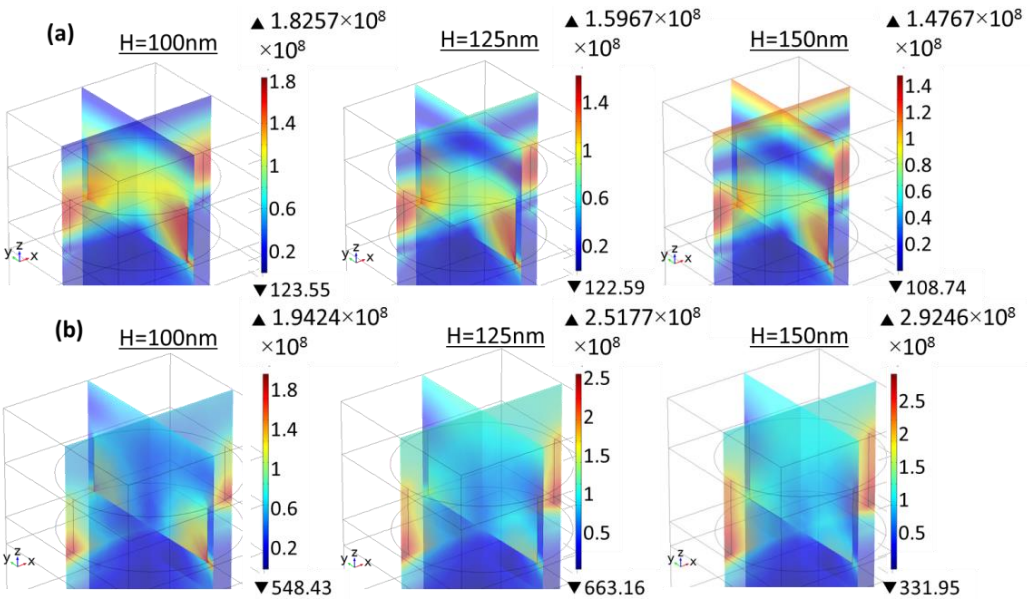

Figure 25 E field distribution for different H and P at λ = 650 nm. (a) P = 300 nm, E couples both into the air and TiO_2 domains, and the strength of the field changes slightly; (b) P = 340 nm, E couples mainly into TiO_2 domain for H = 150 nm, but gets weaker and redistributes into the air domain as H decreases to 100 nm.

In addition to strong peaks showing in Figure 24, all three simulations show small peaks for incident wavelength from 550 nm to 600 nm, and their positions as well as the strength are varied by varying the thickness of Au disks. Since these peaks are far

below the SPR region and can be affected by changing the depth (h) of the nanohole structures (results not shown here), they are most likely to be induced by cavity resonance.

When introducing a new photoactive structure to real application, the reception angle of the structure is another important factor that needs to be investigated in addition to absorption enhancement factor under normal incidence. As a result, incident angle (θ) from 0 to 45 degree are swept with other parameters being t = 25 nm, P = 320 nm and h = 150 nm. Figure 26 shows the AEF mapping with respect to incident wavelength and angle. Taking a comparison between Figure 26 and Figure 24(b), we find that the maximum AEF value can reach 5 for most incident angles at resonance, i.e. 700 ≤ λ ≤ 850 nm. In fact, a closer look at Figure 26 indicates that only a limited region defined by θ ϵ (17, 34) deg and λ ϵ (450, 500) nm gives 70% of original absorption. Besides that, the Au-TiO_2 system exhibits enhanced or similar absorption comparing to TiO_2 without Au in the entire mapping.

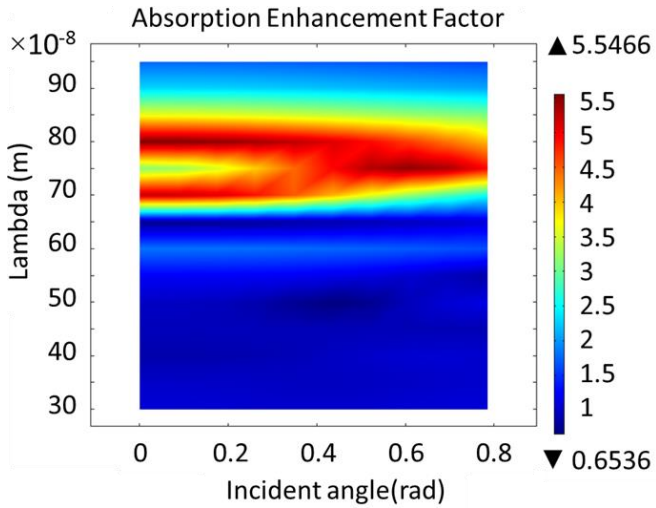

Figure 26 Mapping of absorption enhancement factor with respect to incident angle and incident wavelength at t = 25 nm, P = 320 nm and h = 150 nm.

Further simulation has revealed that the SPR position does not change with h (150 nm to 1500 nm), meaning the SPR effect based on our proposed structure is insensitive to the depth of the initial nanohole structure. Based on this conclusion, we can expect very thin and light film for the electrode. Moreover, by repeating all the simulations

above under TE (transverse electric) modes, we find that every single simulation leads to the same outcomes both qualitatively and quantitatively as under TM modes. This is attributed to the symmetry in x and y dimension of the proposed structure.

3.3 Contribution to Science

This section summarizes the main research results and statements in Chapter 3 and draws the scientific contribution of the current work.

- Theoretical study of mechanism under electrochemical anodization of TiO_2 proves the possibility of forming hemispheric shape on the bottom of nanostructures.
- Well controlled TiO_2 nanotube arrays of 15 µm in length, 120 nm in diameter and 8 nm in wall thickness can be achieved at anodization voltage of 50 V by critical control of anodization time with regard to electrolyte condition.
- Nanocrystalline Au of different morphology can be formed on top of TiO_2 nanotubes via magnetron sputtering; photoactivity and photoelectrical properties of Au-TiO_2 nanostructures are prominently improved as compared to pristine TiO_2 nanotubes.
- Numerical study of interaction between electromagnetic wave and TiO_2 nanostructures helps to better understanding SPR-induced photocurrent enhancement on Au-TiO_2 nanostructures.

4 Conclusion and recommendations for future work

This PhD work has been focused on both theoretical and experimental studies of Au/TiO_2 nanostructures for the purpose of photoelectrochemical water splitting.

One-dimensional anodic TiO_2 nanotubes have been chosen as photoanode for PEC water splitting. The inner diameter, wall thickness and length of nanotubes are well controlled at approximately 120 nm, 8 nm and 15 μm by varying anodization voltage and time corresponding to anodization electrolyte. Simulation was conducted on electric domain in order to investigate the mechanism of electrochemical anodization process. Simulation results proved the possibility of forming hemispheric shape on the bottom of nanostructures due to the existence of nonsolid electrolyte material. From constantly repeated experiments, we noticed that detachment of TNTA membrane from Ti substrate could still happen during or right after anodization despite of careful pre-cleaning procedure. μ, further investigation is needed to explore the issue. For instance, surface circumstance of Ti substrates can be examined before anodization and composition of electrolyte can be identified before and after anodization.

In order to take advantage of SPR and facilitate photo absorption and charge transfer of the photoanode, Au nanoparticles and nanorings have been loaded on TiO_2 nanotube arrays via magnetron sputtering for different time intervals. UV-vis absorption spectrum indicates that all Au/TiO_2 systems exhibit absorption peaks in the visible light region (500-650 nm). Different PEC characterization results suggest that addition of Au, despite of morphology, on TiO_2 nanotubes can accelerate the transfer of photo-generated charge carriers and thus enhance the photocurrent response. In addition, by comparing with previously reported data on Au nanoparticles enhanced photocurrent density, it can be concluded that photocurrent response on TiO_2/Au-nanoparticle systems can be enhanced by increasing the quantity of Au particles. The pros of applying nanoring structures to substitute for nanoparticles is that while holding a comparable PEC enhancement factor, the former is more controllable in terms of geometric dimensions and can be more favourable with regard to industrial application.

In addition to experimental results, numerical simulation has been conducted to further explore SPR effect. Simulation result suggests that the shift in resonant frequency observed on different samples is related to the size, amount and morphology of Au nanocrystalline layer. FEA have also indicated that the ramping up behaviour upon illumination might be related to how the electric field is distributed and how the charge carriers travel and recombine along the longitudinal dimension of TiO_2 nanotubes. Numerical study has not only verified the experimental results but also revealed the difference in SPRs generated from different metallic nanostructures. However, further study is needed to explain more precisely the distinct ramping up behaviour of Au nanocrytalline-coated TiO_2 systems.

Lastly, we have proposed a novel optical structure where Au nanodisks are embedded in titanium dioxide nanohole arrays. Simulation results demonstrated five to seven times light absorption enhancement at resonant wavelength of 700 - 800 nm despite of varied reception angles from 0 to 45 degrees. Furthermore, broad absorption bandwidth can be achieved by optimizing the thickness of embedded Au layer. Such structure will improve the optical absorption performance of TiO_2 nanostructure in the visible light region and at the same time ensure the UV absorption of TiO_2 material. Fabrication process was introduced in Journal paper 2. Practical manufacture and characterization activities should be carried out for verification and test in the future.

Although the published literatures have been directed specifically to PEC water splitting applications, we expect that our Au-nanoring/TNTs and proposed Au-nanodisks/TiO_2 nanohole structures can be beneficial to other PEC performance as well.

References

[1] S. Chen, T. Takata, and K. Domen, "Particulate photocatalysts for overall water splitting," *Nature Reviews Materials,* vol. 2, p. 17050, 2017.

[2] Z. Chen, H. N. Dinh, and E. Miller, *Photoelectrochemical water splitting:* Springer Briefs in Energy, New York, 2013.

[3] P. Roy, S. Berger, and P. Schmuki, "TiO_2 nanotubes: synthesis and applications," *Angewandte Chemie International Edition,* vol. 50, pp. 2904-2939, 2011.

[4] Z. Zhang, L. Zhang, M. N. Hedhili, H. Zhang, and P. Wang, "Plasmonic gold nanocrystals coupled with photonic crystal seamlessly on TiO_2 nanotube photoelectrodes for efficient visible light photoelectrochemical water splitting," *Nano Letters,* vol. 13, pp. 14-20, 2012.

[5] Z. Liu, W. Hou, P. Pavaskar, M. Aykol, and S. B. Cronin, "Plasmon resonant enhancement of photocatalytic water splitting under visible illumination," *Nano Letters,* vol. 11, pp. 1111-1116, 2011.

[6] C. U. Gomes Silva, R. Juárez, T. Marino, R. Molinari, and H. García, "Influence of excitation wavelength (UV or visible light) on the photocatalytic activity of titania containing gold nanoparticles for the generation of hydrogen or oxygen from water," *Journal of the American Chemical Society,* vol. 133, pp. 595-602, 2010.

[7] A. Fujishima, "Electrochemical photolysis of water at a semiconductor electrode," *Nature*, vol. 238, pp. 37-38, 1972.

[8] O. Khaselev and J. A. Turner, "A monolithic photovoltaic-photoelectrochemical device for hydrogen production via water splitting," *Science*, vol. 280, pp. 425-427, 1998.

[9] F. E. Osterloh, "Inorganic nanostructures for photoelectrochemical and photocatalytic water splitting," *Chemical Society Reviews,* vol. 42, pp. 2294-2320, 2013.

[10] T. Hisatomi, J. Kubota, and K. Domen, "Recent advances in semiconductors for photocatalytic and photoelectrochemical water splitting," *Chemical Society Reviews,* vol. 43, pp. 7520-7535, 2014.

[11] D. M. Fabian, S. Hu, N. Singh, F. A. Houle, T. Hisatomi, K. Domen, F. E. Osterloh, and S. Ardo, "Particle suspension reactors and materials for solar-driven water splitting," *Energy & Environmental Science,* vol. 8, pp. 2825-2850, 2015.

[12] A. Kudo and Y. Miseki, "Heterogeneous photocatalyst materials for water splitting," *Chemical Society Reviews,* vol. 38, pp. 253-278, 2009.

[13] X. Chen, S. Shen, L. Guo, and S. S. Mao, "Semiconductor-based photocatalytic hydrogen generation," *Chemical Reviews,* vol. 110, pp. 6503-6570, 2010.

[14] O. Khaselev, A. Bansal, and J. A. Turner, "High-efficiency integrated multijunction photovoltaic/electrolysis systems for hydrogen production," *International Journal of Hydrogen Energy,* vol. 26, pp. 127-132, 2001/02/01, 2001.

[15] S. Licht, B. Wang, S. Mukerji, T. Soga, M. Umeno, and H. Tributsch, "Over 18% solar energy conversion to generation of hydrogen fuel; theory and experiment

for efficient solar water splitting," *International Journal of Hydrogen Energy,* vol. 26, pp. 653-659, 2001/07/01, 2001.

[16] J. Gu, Y. Yan, J. W. Krizan, Q. D. Gibson, Z. M. Detweiler, R. J. Cava, and A. B. Bocarsly, "p-Type $CuRhO_2$ as a self-healing photoelectrode for water reduction under visible light," *Journal of the American Chemical Society,* vol. 136, pp. 830-833, 2014/01/22, 2014.

[17] G. Wang, H. Wang, Y. Ling, Y. Tang, X. Yang, R. C. Fitzmorris, C. Wang, J. Z. Zhang, and Y. Li, "Hydrogen-treated TiO_2 nanowire arrays for photoelectrochemical water splitting," *Nano Letters,* vol. 11, pp. 3026-3033, 2011/07/13, 2011.

[18] X. Yang, A. Wolcott, G. Wang, A. Sobo, R. C. Fitzmorris, F. Qian, J. Z. Zhang, and Y. Li, "Nitrogen-doped ZnO nanowire arrays for photoelectrochemical water splitting," *Nano Letters,* vol. 9, pp. 2331-2336, 2009/06/10, 2009.

[19] J. Su, L. Guo, N. Bao, and C. A. Grimes, "Nanostructured $WO_3/BiVO_4$ heterojunction films for efficient photoelectrochemical water splitting," *Nano Letters,* vol. 11, pp. 1928-1933, 2011/05/11, 2011.

[20] Y. Ling, G. Wang, D. A. Wheeler, J. Z. Zhang, and Y. Li, "Sn-doped hematite nanostructures for photoelectrochemical water splitting," *Nano Letters,* vol. 11, pp. 2119-2125, 2011/05/11, 2011.

[21] Y. H. Ng, A. Iwase, A. Kudo, and R. Amal, "Reducing graphene oxide on a visible-light $BiVO_4$ photocatalyst for an enhanced photoelectrochemical water splitting," *The Journal of Physical Chemistry Letters,* vol. 1, pp. 2607-2612, 2010.

[22] Y. S. Hu, A. Kleiman-Shwarsctein, A. J. Forman, D. Hazen, J. N. Park, and E. W. McFarland, "Pt-doped α-Fe_2O_3 thin films active for photoelectrochemical water splitting," *Chemistry of Materials,* vol. 20, pp. 3803-3805, 2008.

[23] Y. C. Pu, G. Wang, K. D. Chang, Y. Ling, Y. K. Lin, B. C. Fitzmorris, C. M. Liu, X. Lu, Y. Tong, J. Z. Zhang, Y. J. Hsu, and Y. Li, "Au nanostructure-decorated TiO_2 nanowires exhibiting photoactivity across entire UV-visible region for photoelectrochemical water splitting," *Nano Letters,* vol. 13, pp. 3817-3823, 2013.

[24] Y. Hou, F. Zuo, A. Dagg, and P. Feng, "Visible light-driven α-Fe_2O_3 nanorod/graphene/$BiV_{1-x}Mo_xO_4$ core/shell heterojunction array for efficient photoelectrochemical water splitting," *Nano Letters,* vol. 12, pp. 6464-6473, 2012.

[25] Y. Qiu, S. F. Leung, Q. Zhang, B. Hua, Q. Lin, Z. Wei, K. H. Tsui, Y. Zhang, S. Yang, and Z. Fan, "Efficient photoelectrochemical water splitting with ultrathin films of hematite on three-dimensional nanophotonic structures," *Nano Letters,* vol. 14, pp. 2123-2129, 2014.

[26] M. T. Mayer, C. Du, and D. Wang, "Hematite/Si nanowire dual-absorber system for photoelectrochemical water splitting at low applied potentials," *Journal of the American Chemical Society,* vol. 134, pp. 12406-12409, 2012/08/01, 2012.

[27] Y. Qiu, K. Yan, H. Deng, and S. Yang, "Secondary branching and nitrogen doping of ZnO nanotetrapods: Building a highly active network for photoelectrochemical water splitting," *Nano Letters,* vol. 12, pp. 407-413, 2012/01/11, 2012.

[28] Y. Li, T. Takata, D. Cha, K. Takanabe, T. Minegishi, J. Kubota, and K. Domen, "Vertically aligned Ta_3N_5 nanorod arrays for solar-driven photoelectrochemical water splitting," *Advanced Materials,* vol. 25, pp. 125-131, 2013.

[29] Y. Zhao, N. Hoivik, and K. Wang, "Recent advance on engineering titanium dioxide nanotubes for photochemical and photoelectrochemical water splitting," *Nano Energy,* vol. 30, pp. 728-744, 2016.

[30] T. Inoue and T. Yamase, "Photoelectrochemical cell using SiC for water splitting," *Chemistry Letters*, vol. 14, pp. 869-872, 1985.

[31] K. Iwashina and A. Kudo, "Rh-doped $SrTiO_3$ photocatalyst electrode showing cathodic photocurrent for water splitting under visible-light irradiation," *Journal of the American Chemical Society,* vol. 133, pp. 13272-13275, 2011/08/31, 2011.

[32] Y. Liu, Y. Gu, X. Yan, Z. Kang, S. Lu, Y. Sun, and Y. Zhang, "Design of sandwich-structured ZnO/ZnS/Au photoanode for enhanced efficiency of photoelectrochemical water splitting," *Nano Research*, vol. 8, pp. 2891-2900, 09/01, 2015.

[33] B. O'Regan and M. Grätzel, "A low-cost, high-efficiency solar cell based on dye-sensitized colloidal TiO_2 films," *Nature*, vol. 353, p. 737, 10/24, 1991.

[34] R. Beranek, H. Tsuchiya, T. Sugishima, J. Macak, L. Taveira, S. Fujimoto, et al., "Enhancement and limits of the photoelectrochemical response from anodic TiO_2 nanotubes," *Applied Physics Letters,* vol. 87, p. 243114, 2005.

[35] P. Hoyer, "Formation of a titanium dioxide nanotube array," *Langmuir,* vol. 12, pp. 1411-1413, 1996.

[36] M. S. Sander, M. J. Cote, W. Gu, B. M. Kile, and C. P. Tripp, "Template-assisted fabrication of dense, aligned arrays of titania nanotubes with well-controlled dimensions on substrates," *Advanced Materials,* vol. 16, pp. 2052-2057, 2004.

[37] H. Shin, D. K. Jeong, J. Lee, M. M. Sung, and J. Kim, "Formation of TiO_2 and ZrO_2 nanotubes using atomic layer deposition with ultraprecise control of the wall thickness," *Advanced Materials,* vol. 16, pp. 1197-1200, 2004.

[38] M. Knez, K. Nielsch, and L. Niinistö, "Synthesis and surface engineering of complex nanostructures by atomic layer deposition," *Advanced Materials,* vol. 19, pp. 3425-3438, 2007.

[39] T. Kasuga, M. Hiramatsu, A. Hoson, T. Sekino, and K. Niihara, "Formation of titanium oxide nanotube," *Langmuir*, vol. 14, pp. 3160-3163, 1998.

[40] V. Zwilling, E. Darque-Ceretti, A. Boutry-Forveille, D. David, M. Y. Perrin, and M. Aucouturier, "Structure and physicochemistry of anodic oxide films on titanium and TA_6V alloy," *Surface and Interface Analysis,* vol. 27, pp. 629-637, 1999.

[41] V. Zwilling, M. Aucouturier, and E. Darque-Ceretti, "Anodic oxidation of titanium and TA_6V alloy in chromic media. An electrochemical approach," *Electrochimica Acta,* vol. 45, pp. 921-929, 1999.

[42] S. P. Albu, A. Ghicov, J. M. Macak, R. Hahn, and P. Schmuki, "Self-organized, free-standing TiO_2 nanotube membrane for flow-through photocatalytic applications," *Nano Letters,* vol. 7, pp. 1286-1289, 2007/05/01, 2007.

[43] D. V. Bavykin, A. N. Kulak, and F. C. Walsh, "Control over the hierarchical structure of titanate nanotube agglomerates," *Langmuir*, vol. 27, pp. 5644-5649, 2011/05/03, 2011.

[44] N. Liu, X. Chen, J. Zhang, and J. W. Schwank, "A review on TiO_2-based nanotubes synthesized via hydrothermal method: Formation mechanism, structure modification, and photocatalytic applications," *Catalysis Today,* vol. 225, pp. 34-51, 2014/04/15, 2014.

[45] S. Singh, M. Festin, W. R. T. Barden, L. Xi, J. T. Francis, and P. Kruse, "Universal method for the fabrication of detachable ultrathin films of several transition metal oxides," *ACS Nano,* vol. 2, pp. 2363-2373, 2008/11/25, 2008.

[46] H.-c. Liang and X.-z. Li, "Effects of structure of anodic TiO_2 nanotube arrays on photocatalytic activity for the degradation of 2, 3-dichlorophenol in aqueous solution," *Journal of Hazardous Materials,* vol. 162, pp. 1415-1422, 2009.

[47] K. Rajeshwar, *Fundamentals of semiconductor electrochemistry and photoelectrochemistry*: Encyclopedia of electrochemistry, 2007.

[48] M. Junghänel, *Novel aqueous electrolyte films for hole conduction in dye sensitized solar cells and development of an electron transport model*: Freie Universität Berlin, 2007.

[49] G. L. Chiarello, A. Zuliani, D. Ceresoli, R. Martinazzo, and E. Selli, "Exploiting the photonic crystal properties of TiO_2 nanotube arrays to enhance photocatalytic hydrogen production," *ACS Catalysis,* vol. 6, 2016.

[50] F. Nunzi and F. De Angelis, "DFT investigations of formic acid adsorption on single-wall TiO_2 nanotubes: effect of the surface curvature," *The Journal of Physical Chemistry C,* vol. 115, pp. 2179-2186, 2010.

[51] K. Du, G. Liu, M. Li, C. Wu, X. Chen, and K. Wang, "Electrochemical reduction and capacitance of hybrid titanium dioxides-nanotube arrays and “nanograss”," *Electrochimica Acta,* vol. 210, pp. 367-374, 2016.

[52] T. Umebayashi, T. Yamaki, H. Itoh, and K. Asai, "Band gap narrowing of titanium dioxide by sulfur doping," *Applied Physics Letters,* vol. 81, pp. 454-456, 2002.

[53] C. W. Dunnill and I. P. Parkin, "Nitrogen-doped TiO_2 thin films: photocatalytic applications for healthcare environments," *Dalton Transactions,* vol. 40, pp. 1635-1640, 2011.

[54] X. Chen, L. Liu, P. Y. Yu, and S. S. Mao, "Increasing solar absorption for photocatalysis with black hydrogenated titanium dioxide nanocrystals," *Science,* vol. 331, pp. 746-50, 02/11, 2011.

[55] W. Zhu, X. Liu, H. Liu, D. Tong, J. Yang, and J. Peng, "Coaxial heterogeneous structure of TiO_2 nanotube arrays with CdS as a superthin coating synthesized via modified electrochemical atomic layer deposition," *Journal of the American Chemical Society,* vol. 132, pp. 12619-12626, 2010/09/15, 2010.

[56] C. W. Lai and S. Sreekantan, "Preparation of hybrid WO_3-TiO_2 nanotube photoelectrodes using anodization and wet impregnation: Improved water-splitting hydrogen generation performance," *International Journal of Hydrogen Energy,* vol. 38, pp. 2156-2166, 2013.

[57] M. Gholami, M. Qorbani, O. Moradlou, N. Naseri, and A. Z. Moshfegh, "Optimal Ag_2S nanoparticle incorporated TiO_2 nanotube array for visible water splitting," *RSC Advances,* vol. 4, pp. 7838-7844, 2014.

[58] S. Linic, P. Christopher, and D. B. Ingram, "Plasmonic-metal nanostructures for efficient conversion of solar to chemical energy," *Nature Materials,* vol. 10, pp. 911-921, 2011.

[59] J. P. O'Sullivan and G. C. Wood, *The morphology and mechanism of formation of porous anodic films on aluminium*: Proceedings of the Royal Society of London. A. Mathematical and Physical Sciences, 1970.

[60] Y. Zhao, N. Hoivik, and K. Wang, "Study of TiO_2 Nanotube Formation Mechanisms by Simulation on Electric Domain," *ECS Transactions,* vol. 61, pp. 9-13, 2014.

[61] K. Shankar, G. K. Mor, A. Fitzgerald, and C. A. Grimes, "Cation effect on the electrochemical formation of very high aspect ratio TiO_2 nanotube arrays in formamide-water mixtures," *The Journal of Physical Chemistry C,* vol. 111, pp. 21-26, 2007/01/01, 2007.

[62] J. M. Macak, H. Tsuchiya, L. Taveira, S. Aldabergerova, and P. Schmuki, "Smooth anodic TiO_2 nanotubes," *Angewandte Chemie International Edition,* vol. 44, pp. 7463-7465, 2005.

[63] F. Mohammadpour, M. Altomare, S. So, K. Lee, M. Mokhtar, A. Alshehri, and P. Schmuki, "High-temperature annealing of TiO_2 nanotube membranes for efficient dye-sensitized solar cells," *Semiconductor Science and Technology,* vol. 31, p. 014010, 2015.

[64] A. Tighineanu, T. Ruff, S. Albu, R. Hahn, and P. Schmuki, "Conductivity of TiO_2 nanotubes: influence of annealing time and temperature," *Chemical Physics Letters,* vol. 494, pp. 260-263, 2010.

[65] A. Mazare, G. Totea, C. Burnei, P. Schmuki, I. Demetrescu, and D. Ionita, "Corrosion, antibacterial activity and haemocompatibility of TiO_2 nanotubes as a function of their annealing temperature," *Corrosion Science,* vol. 103, pp. 215-222, 2016.

[66] Y. Zhao, N. Hoivik, and K. Wang, "Photoconductivity of Au-coated TiO_2 nanotube arrays," *IEEE 14th International Conference, 2014,* pp. 180-183, 2014.

[67] R. F. Egerton, *Physical principles of electron microscopy*: Springer, 2005.

[68] R. A. Awang, S. H. El-Gohary, N. H. Kim, and K. M. Byun, "Enhancement of field-analyte interaction at metallic nanogap arrays for sensitive localized surface plasmon resonance detection," *Applied optics,* vol. 51, pp. 7437-7442, 2012.

[69] S. Shuang, R. Lv, Z. Xie, and Z. Zhang, "Surface plasmon enhanced photocatalysis of Au/Pt-decorated TiO_2 nanopillar arrays," *Scientific reports,* vol. 6, p. 26670, 2016.

[70] Q. Wang, J.-E. Moser, and M. Grätzel, "Electrochemical impedance spectroscopic analysis of dye-sensitized solar cells," *The Journal of Physical Chemistry B,* vol. 109, pp. 14945-14953, 2005.

[71] M. E. Orazem and B. Tribollet, *Electrochemical impedance spectroscopy* vol. 48: John Wiley & Sons, 2011.

[72] Z. Xu, Y. Lin, M. Yin, H. Zhang, C. Cheng, L. Lu, X. Xue, H. J. Fan, X. Chen, and D. Li, "Understanding the enhancement mechanisms of surface plasmon-mediated photoelectrochemical electrodes: A case study on Au nanoparticle decorated TiO_2 nanotubes," *Advanced Materials Interfaces,* vol. 2, 2015.

[73] Y. Nishijima, K. Ueno, Y. Yokota, K. Murakoshi, and H. Misawa, "Plasmon-assisted photocurrent generation from visible to near-infrared wavelength using a Au-nanorods/TiO_2 electrode," *The Journal of Physical Chemistry Letters,* vol. 1, pp. 2031-2036, 2010.

[74] P. Christopher, D. B. Ingram, and S. Linic, "Enhancing photochemical activity of semiconductor nanoparticles with optically active Ag nanostructures: photochemistry mediated by Ag surface plasmons," *The Journal of Physical Chemistry C,* vol. 114, pp. 9173-9177, 2010.

[75] D. B. Ingram and S. Linic, "Water splitting on composite plasmonic-metal/semiconductor photoelectrodes: Evidence for selective plasmon-induced formation of charge carriers near the semiconductor surface," *Journal of the American Chemical Society,* vol. 133, pp. 5202-5205, 2011/04/13, 2011.

[76] S. E. Han and G. Chen, "Optical absorption enhancement in silicon nanohole arrays for solar photovoltaics," *Nano Letters,* vol. 10, pp. 1012-1015, 2010.

[77] W. Wang, S. Wu, K. Reinhardt, Y. Lu, and S. Chen, "Broadband light absorption enhancement in thin-film silicon solar cells," *Nano Letters,* vol. 10, pp. 2012-2018, 2010.

[78] H. A. Atwater and A. Polman, "Plasmonics for improved photovoltaic devices," *Nature Materials,* vol. 9, pp. 205-213, 2010.

[79] S. A. Maier, *Plasmonics: fundamentals and applications*: Springer Science & Business Media, 2007.

[80] R. A. Pala, J. White, E. Barnard, J. Liu, and M. L. Brongersma, "Design of plasmonic thin-film solar cells with broadband absorption enhancements," *Advanced Materials,* vol. 21, pp. 3504-3509, 2009.

[81] C. Rockstuhl, S. Fahr, and F. Lederer, "Absorption enhancement in solar cells by localized plasmon polaritons," *Journal of applied physics,* vol. 104, p. 123102, 2008.

[82] J. W. Marvin and J. Weber, *Handbook of optical materials*: the CRC Press LLC, 2003.

[83] E. D. Palik, *Handbook of optical constants of solids*: Academic press, 1998.

[84] B. Wang, T. Gao, and P. W. Leu, "Broadband light absorption enhancement in ultrathin film crystalline silicon solar cells with high index of refraction nanosphere arrays," *Nano Energy,* vol. 19, pp. 471-475, 2016.

[85] S. Eustis and M. A. El-Sayed, "Why gold nanoparticles are more precious than pretty gold: noble metal surface plasmon resonance and its enhancement of the radiative and nonradiative properties of nanocrystals of different shapes," *Chemical Society Reviews,* vol. 35, pp. 209-217, 2006.

Papers omitted from online publication due to publisher's restrictions

Appendix I - Diffraction data

Pattern : 00-044-1294 *Radiation =* 1.540598 *Quality :* High

Ti

Titanium

Lattice : Hexagonal *Mol. weight =* 47.90

S.G. : P63/mmc (194) *Volume [CD] =* 35.30

a = 2.95050 *Dx =* 4.506

c = 4.68260

Z = 2 *I/Icor =* 0.90

2th	i	h	k	l
35.094	25	1	0	0
38.422	30	0	0	2
40.171	100	1	0	1
53.005	13	1	0	2
62.951	11	1	1	0
70.662	11	1	0	3
74.160	1	2	0	0
76.221	9	1	1	2
77.370	6	2	0	1
82.292	1	0	0	4
86.762	1	2	0	2
92.732	1	1	0	4
102.364	2	2	0	3
105.802	1	2	1	0
109.046	4	2	1	1
114.283	3	1	1	4
119.260	1	2	1	2

Additional Patterns: Validated by calculated pattern. To replace 00-005-0682. Color: Gray. General Comments: Average relative standard deviation in intensity of the ten strongest reflections for three specimen mounts = 6.7%. Component of pyrotechnic boom powders. Sample Source or Locality: Sample was obtained from A.D. Mackay Inc. Unit Cell Data Source: Powder Diffraction. Data collection flag: Ambient.

Sailer, R., McCarthy, G., North Dakota State University, Fargo, North Dakota, USA., ICDD Grant-in-Aid (1993)

CAS Number: 7440-32-6

Radiation : CuKα1 *Filter :* Monochromator crystal

Lambda : 1.54056 *d-sp :* Diffractometer

SS/FOM : F17=414(0.0020,17)

Pattern : 00-021-1272 **Radiation =** 1.540598 **Quality :** High

TiO_2

Titanium Oxide
Also called: anatase, Anatase, syn

Lattice : Body-centered tetragonal ***Mol. weight =*** 79.90

S.G. : I41/amd (141) ***Volume [CD] =*** 136.31

a = 3.78520 ***Dx =*** 3.893

c = 9.51390

Z = 4 ***I/Icor =*** 3.30

Additional Patterns: See PDF 01-071-1166. Validated by calculated pattern. Color: Colorless. General Comments: Pattern reviewed by Holzer, J., McCarthy, G., North Dakota State Univ, Fargo, North Dakota, USA, ICDD Grant-in-Aid (1990). Agrees well with experimental and calculated patterns. Polymorphism/Phase Transition: Anatase and another polymorph, brookite (orthorhombic), are converted to rutile (tetragonal) by heating above 700 C. Sample Source or Locality: Sample obtained from National Lead Co., South Amboy, New Jersey, USA. Temperature of Data Collection: Pattern taken at 298 K. Unit Cell Data Source: Powder Diffraction.
Data collection flag: Ambient.

2th	i	h	k	l
25.281	100	1	0	1
36.947	10	1	0	3
37.801	20	0	0	4
38.576	10	1	1	2
48.050	35	2	0	0
53.891	20	1	0	5
55.062	20	2	1	1
62.121	4	2	1	3
62.690	14	2	0	4
68.762	6	1	1	6
70.311	6	2	2	0
74.031	2	1	0	7
75.032	10	2	1	5
76.020	4	3	0	1
80.727	2	0	0	8
82.139	2	3	0	3
82.662	6	2	2	4
83.149	4	3	1	2
93.220	2	2	1	7
94.181	4	3	0	5
95.143	4	3	2	1
98.318	2	1	0	9
99.804	2	2	0	8
101.221	2	3	2	3
107.448	4	3	1	6
108.963	4	4	0	0
112.840	2	3	0	7
113.861	2	3	2	5
114.909	2	4	1	1
118.439	4	2	1	9
120.104	2	2	2	8
121.725	2	4	1	3
122.336	2	4	0	4
131.035	2	4	2	0
135.998	2	3	2	7
137.391	4	4	1	5
143.887	2	3	0	9
150.039	4	4	2	4
152.633	2	0	0	12

Natl. Bur. Stand. (U.S.) Monogr. 25, volume 7, page 82 (1969)

Radiation : ***Filter :***

d-sp : Not given

SS/FOM : F30= 75(0.0111,35)

Pattern : 00-004-0784 ***Radiation =*** 1.540598 ***Quality :*** High

Au

Gold
Gold, syn

2th	*i*	*h*	*k*	*l*
38.185	100	1	1	1
44.393	52	2	0	0
64.578	32	2	2	0
77.549	36	3	1	1
81.724	12	2	2	2
98.137	6	4	0	0
110.802	23	3	3	1
115.264	22	4	2	0
135.422	23	4	2	2

Lattice : Face-centered cubic ***Mol. weight =*** 196.97

S.G. : Fm-3m (225) ***Volume [CD] =*** 67.85

a = 4.07860 ***Dx =*** 19.283

Dm = 19.300

Z = 4

Analysis: Spectrographic analysis (%): Si 0.001, Ca 0.001, Ag 0.001(?). Color: Yellow metallic. Melting Point: 1334.6-1336.2 K. Opaque Optical Data: Opaque mineral optical data on specimen from unspecified locality: RR2Re=71.6, Disp.= 16, VHN100=53-58, Color values=.384, .391, 72.7, Ref.: IMA Commission on Ore Microscopy QDF. Sample Source or Locality: Sample purified at NBS, Gaithersburg, Maryland, USA and is about 99.997% Au. Temperature of Data Collection: Pattern taken at 299 K. Unit Cell Data Source: Powder Diffraction. Data collection flag: Ambient.

Swanson, Tatge., Natl. Bur. Stand. (U.S.), Circ. 539, volume I, page 33 (1953)

CAS Number: 7440-57-5

Radiation : CuKα1 ***Filter :*** Beta

Lambda : 1.54056 ***d-sp :*** Not given

SS/FOM : F9=129(0.0070,9)